



# Geochemical, sedimentological and microbial diversity in two thermokarst lakes of far Eastern Siberia

Ove H. Meisel<sup>1</sup> · Ruud Rijkers<sup>1</sup> · Joshua F. Dean<sup>2</sup> · Michiel H. in 't Zandt<sup>1</sup> · Jacobus van Huissteden<sup>1</sup> · Trofim C. Maximov · Sergey V. Karsanaev<sup>3</sup> · Luca Beelli Marchesini<sup>4</sup> · Arne Goovaerts · Lukas Wacker<sup>5</sup> · Gert-Jan Reichart<sup>6</sup> · Steven Bouillon<sup>7</sup> · Cornelia U. Welte<sup>8</sup> · Mike S. M. Jetten<sup>9</sup> · Jorien E. Vonk<sup>10</sup> · Han Dolman<sup>10</sup>

Received: 27 October 2022 / Accepted: 31 July 2023 / Published online: 23 August 2023  
© The Author(s) 2023

**Abstract** Thermokarst lakes are important conduits for organic carbon sequestration, soil organic matter (soil-OM) decomposition and release of atmospheric greenhouse gases in the Arctic. They can be classified as either floating-ice lakes, which sustain a zone of unfrozen sediment (talik) at the lakebed year-round, or as bedfast-ice lakes, which freeze all the way to the lakebed in winter. Another key characteristic of thermokarst lakes are their eroding

shorelines, depending on the surrounding landscape, they can play a major role in supplying the lakebeds with sediment and OM. These differences in winter ice regime and eroding shorelines are key factors which determine the quantity and quality of OM in thermokarst lake sediments. We used an array of physical, geochemical, and microbiological tools to identify the differences in the environmental conditions, sedimentary characteristics, carbon stocks and microbial community compositions in the sediments of a bedfast-ice and a floating-ice lake in Far East Siberia with different eroding shorelines. Our data show strong differences across most of the measured parameters between the two lakes. For example, the

Handling Editor: Brian Branfireun.

**Supplementary Information** The online version contains supplementary material available at <https://doi.org/10.1007/s10533-023-01076-1>.

O. H. Meisel · J. van Huissteden · J. E. Vonk (✉) · H. Dolman

Faculty of Science, Earth and Climate, Vrije Universiteit Amsterdam, 1081 HV Amsterdam, The Netherlands  
e-mail: j.e.vonk@vu.nl

O. H. Meisel · M. H. in 't Zandt · G.-J. Reichart · C. U. Welte · M. S. M. Jetten · J. E. Vonk · H. Dolman  
Netherlands Earth System Science Centre (NESSC), Utrecht University, 3584 CS Utrecht, The Netherlands

R. Rijkers  
Department of Ecological Science, Amsterdam Institute for Life and Environment, Vrije Universiteit Amsterdam, 1081 HV Amsterdam, The Netherlands

J. F. Dean  
School of Geographical Sciences, University of Bristol, Bristol BS8 1SS, UK

M. H. in 't Zandt · C. U. Welte · M. S. M. Jetten  
Department of Microbiology, Radboud Institute for Biological and Environmental Sciences, Radboud University, Heyendaalseweg 135, 6525 AJ Nijmegen, The Netherlands

M. H. in 't Zandt  
Soil Biology Group, Wageningen University, 6708 PB Wageningen, The Netherlands

T. C. Maximov · S. V. Karsanaev  
Institute for Biological Problems of the Cryolithozone, Siberian Branch Russian Academy of Sciences, Yakutsk, Russian Federation

T. C. Maximov · S. V. Karsanaev  
North-Eastern Federal University, Yakutsk, Russian Federation

floating-ice lake contains considerably lower amounts of sediment organic matter and dissolved organic carbon, both of which also appear to be more degraded in comparison to the bedfast-ice lake, based on their stable carbon isotope composition ( $\delta^{13}\text{C}$ ). We also document clear differences in the microbial community composition, for both archaea and bacteria. We identified the lake water depth (bedfast-ice vs. floating-ice) and shoreline erosion to be the two most likely main drivers of the sedimentary, microbial and biogeochemical diversity in thermokarst lakes. With ongoing climate warming, it is likely that an increasing number of lakes will shift from a bedfast- to a floating-ice state, and that increasing levels of shoreline erosion will supply the lakes with sediments. Yet, still little is known about the physical, biogeochemical and microbial differences in the sediments of these lake types and how different eroding shorelines impact these lake systems.

**Keywords** Thermokarst lakes · Far East Siberia · Arctic permafrost · Yedoma · SOC · Microbial diversity

---

L. Belleli Marchesini  
Forest Ecology Unit, Research and Innovation Centre,  
Fondazione Edmund Mach, 38010 San Michele all'Adige,  
Italy

A. Goovaerts · S. Bouillon  
Department of Earth and Environmental Sciences, KU  
Leuven, 3000 Leuven, Belgium

L. Wacker  
Ion Beam Laboratory, Department of Physics, ETH  
Zürich, 8093 Zurich, Switzerland

G.-J. Reichart · H. Dolman  
Department of Ocean Systems, NIOZ-Royal Netherlands  
Institute for Sea Research, 1790 AB Den Burg,  
The Netherlands

G.-J. Reichart  
Department of Earth Sciences, Faculty of Geosciences,  
Utrecht University, 3508 TA Utrecht, The Netherlands

C. U. Welte · M. S. M. Jetten  
Soehngen Institute of Anaerobic Microbiology, Radboud  
University, Heyendaalseweg 135, 6525 AJ Nijmegen,  
The Netherlands

## Introduction

Arctic permafrost regions store about 50% of the global soil organic carbon (soil-OC) pool (Kuhry et al. 2010), especially near the surface (0–3 m) with an estimated  $1307 \pm 170$  Pg of soil-OC in the northern circumpolar permafrost region alone (Hugelius et al. 2014). A large fraction of this soil-OC is still decoupled from the active carbon cycle and protected from extensive degradation because of freezing temperatures, but strong ongoing climate warming in the Arctic (Jansen et al. 2020) increasingly exposes these soils to thaw (Heslop et al. 2020). The decay of permafrost often occurs in places that are naturally exposed to physical, thermal and environmental forces, such as riverbanks, coastlines, lake shorelines or topographic slopes which allow exposure of the frozen ground (Ballantyne 2018).

Thermokarst lakes are hotspots of rapid permafrost thaw. Here, organic matter (OM) in lakebed sediments, underlying permafrost soils and along eroding shorelines can degrade to greenhouse gases (GHGs) (Walter et al. 2007; van Huissteden 2020). Due to their high abundance and widespread distribution in tundra landscapes, thermokarst lakes play an important role in the Arctic GHG balance (in 't Zandt et al. 2020). The Northeast Siberian coastal lowlands for example are widely covered by small and large lakes which regionally make up more than 40% of the land surface area (Grosse et al. 2013). Thermokarst lakes impact the Arctic carbon budget since they can act both, as sinks which sequester OC (Schirmermeister et al. 2011) at the lakebed, or as sources through the release of GHGs (Zimov et al. 1997; Matveev et al. 2016) depending on timescales, current climatic, hydrological and local geological conditions (Walter Anthony et al. 2014; Webb et al. 2022). The main sediment (and associated OM) source of thermokarst lakes is allochthonous material that is eroded along their shorelines. Whether the lakes sequester OM or act as catalyst for OM decomposition is highly dependent on their rates of sediment deposition (Walvoord et al. 2019).

Sediment temperatures at the lakebed of thermokarst lakes are strongly controlled by their lake ice regime, which describes two different states of their environmental conditions during winter (Ling and Zhang 2003). Firstly, bedfast-ice lakes that freeze all the way to their lakebed during the

winter months, they are shallower than the local maximum winter ice thickness (Arp et al. 2012). Secondly, floating-ice lakes that are deep enough to remain unfrozen at the lakebed also during the peak of winter (Arp et al. 2012). During the summer months, the lakes transfer heat from their water body to the underlying permafrost ground below the lakebed, which gradually thaws the underlying soil over time. This can cause large-scale thermokarst subsidence of the lakebed since the underlying ice-rich permafrost soil can contain 50–90 vol% ice (Nitzbon et al. 2020; Windirsch et al. 2020). During winter, this thawed subsoil naturally refreezes again below bedfast-ice lakes. Over time, ongoing soil subsidence below the lakebed and rising lake water levels can deepen bedfast-ice lakes to such an extent that they exceed the local maximum winter ice thickness. Once this threshold is exceeded, the lake water and the uppermost lake sediment and thawed permafrost soil at the lakebed will remain unfrozen year-round and result in floating-ice lake formation (Arp et al. 2012). Over time, zones of unfrozen ground (taliks) can form below thermokarst lakes and reach vertically 95 m below the lakebed (Schwamborn et al. 2000). The sediment organic carbon (SOC) contained in the lake sediment and thawed permafrost soil of an active talik is no longer subjected to the annual freezing cycle and is exposed to increased year-round microbial activity, resulting in increased degradation of sediment organic matter (SOM) stocks (Walter Anthony et al. 2018; Jongejans et al. 2021).

The conditions for carbon degradation through microbial activity are generally more favorable in floating-ice lakes than in bedfast-ice lakes since its taliks are not frozen throughout the winter. OC degradation through complex microbial networks and CH<sub>4</sub> production by methanogenic archaea that occurs under anoxic conditions are both positively affected by increased temperatures (Wik et al. 2014; Thornton et al. 2015). Therefore, it is likely, that GHG fluxes from floating-ice lake systems may increase, since microbial activity responds positively to both, increased temperatures (here during the winter season) and increased availability of SOM and nutrients (here from shoreline erosion) (Walter Anthony et al. 2014; de Jong et al. 2018; in 't Zandt et al. 2020). Wik et al. (2016) estimated that CH<sub>4</sub> emissions from northern lakes will increase 20–54% by 2100 if

ice-free conditions on the lakes are extended by only 20 days.

So far, the differences in carbon stocks, sediment properties and microbial community compositions within and between these specific thermokarst lake types remain understudied. Jones et al. (2018) emphasize that most lake systems, which includes thermokarst lakes, are internally heterogeneous, and so far they are not well constrained biochemically (Arsenault et al. 2022). For a better assessment of the OC dynamics and eventually the potential future impact on the Arctic GHG balance, more studies and data are key to better understand the intra- and inter-lake variability of these different lake types. Furthermore, there is a growing need to include biogeochemical and microbiological processes in GHG models for specific environments like wetlands (Chadburn et al. 2020). To model thermokarst lake systems will require field data as presented in this study that can provide input variables.

Here, we investigated sediment cores from four sites located in the Northeast Siberian coastal lowlands; one core from a bedfast-ice lake, within a flat tundra location surrounded by peaty soil, and three cores from a floating-ice lake, which also borders an actively eroding permafrost cliff. The focus was on the role of ice regime and allochthonous sediment input on the lake sediment characteristics and its impact on the carbon dynamics in these lakes. We used *sedimentological* (grainsize, gamma-ray bulk density ( $\rho_{\gamma\text{-ray}}$ ), magnetic susceptibility (MS), porewater content), *geochemical* (loss-on-ignition (LOI), dissolved organic carbon (DOC) concentration, soil-OC/SOC and DOC stable carbon isotope values ( $\delta^{13}\text{C}_{\text{org}}$ ,  $\delta^{13}\text{C}_{\text{DOC}}$ ), radiocarbon dating ( $^{14}\text{C}$ ), X-ray fluorescence (XRF) elemental composition) and *microbiological* (16S rRNA gene amplicon sequencing) analyses to create the data base for this study. We aimed to measure a suite of variables to characterize and understand the sedimentological and biogeochemical drivers within two distinct thermokarst lakes. The study of the sediment dynamics in thermokarst lake systems is important considering the likelihood of increasing shifts from bedfast- to floating-ice regimes (Arp et al. 2012) and likely increasing shoreline erosion rates (Jones et al. 2011). These developments might increase the input of eroded OM into thermokarst lake systems and its decomposition rates at the lakebeds. We here document the differences between

two thermokarst lake systems which are likely due to a combination of these two main drivers of lake ice regime and shoreline erosion. While in this study we cannot quantify to what extent these drivers impact the lake sediment and its SOC in proportion to each other we still see clear indications that both ice regime and shoreline erosion play important roles.

## Methodology

### Field site

The study area is in the Kytalyk National Park (Национальный парк Кыталык) in the Russian

Republic of Yakutia. It is situated 480 km above the Arctic Circle along the northern bank of the Berelkh (Бөрөлөх) river (Fig. 1) which merges with the larger Indigirka (Инди́гирка) river near the town of Chokurdakh (Чокурда́х). The field site is situated within the largest and most continuous permafrost region of the planet (Strauss et al. 2017) which contains the largest existing yedoma soil deposits. Yedoma is a Pleistocene-aged soil of organic-rich loess with an average soil-OC content of 2–4 wt%, it contains 50–90% of ground ice and is up to 50 m thick and especially common to the tundra of Far East Siberia (Walter et al. 2006; Jones et al. 2011; Schirmermeister et al. 2013; Murton et al. 2017; Windirsch et al. 2020).

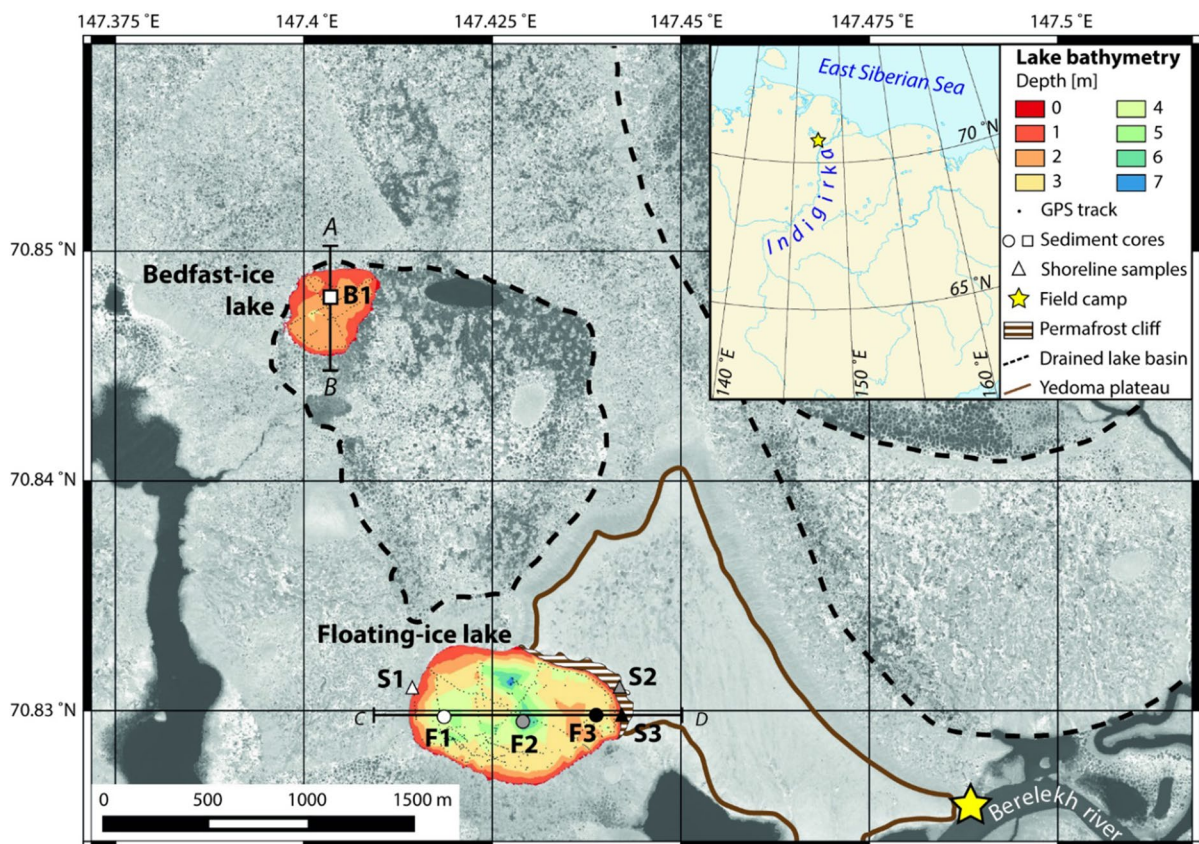


**Fig. 1** Field site map of the study area in the Kytalyk National Park. Bathymetry maps for the floating-ice and bedfast-ice lake are displayed with the sediment core locations B1 (box), F1–F3 (circles), shoreline samples S1–S3 (triangles) and the field camp location (star icon). Geographic features such as drained lake basins (dashed lines), a yedoma plateau (solid line) and an eroding permafrost cliff (striped area) are highlighted. The ver-

tical (A, B) and horizontal (C, D) profile lines across the lakes show the locations of the lake cross section profiles in Fig. 9. The underlying satellite image is from WorldView © 2019 MAXAR (15 July 2015). The small overview map was created with the Generic Mapping Tool (6.1.1.). The field site map was compiled in QGIS 3.16.0

The study area mostly contains flat tundra landscapes and lies 11 m above sea level. In the near vicinity of the field camp the highest elevation point is reached by a 25 m high Late Pleistocene-aged yedoma plateau (van Huissteden et al. 2021). Meteorological data from 2005 to 2020 of the Chokurdakh airport weather station (WMO number 21946) show that the daily mean air temperature is  $-11.5$  °C while the coldest month is January (mean  $-32.6$  °C) and the warmest month is July (mean  $10.4$  °C) ([https://rp5.ru/Weather\\_archive\\_in\\_Chokurdakh\\_\(airport\)](https://rp5.ru/Weather_archive_in_Chokurdakh_(airport)), accessed 10 Oct 2022). Stationary water bodies like ponds and lakes typically have frozen surfaces from November until April in the study area.

The wider area of the Kytalyk field site is covered by large numbers of ponds and lakes (30%) and drained lake basins (38%) (Siewert et al. 2015). Low-lying areas (e.g. drained lake basins) are mainly covered by characteristic tundra vegetation of *Betula nana*, mosses and lichens; elevated areas (e.g. yedoma plateaus) are dominated by tussock-sedge (*Eriophorum vaginatum*); water-locked depressions (e.g. pond areas) are dominated by *Sphagnum* spp., *Eriophorum angustifolium* and *Carex* spp. (Iturrate-Garcia et al. 2020; Magnússon et al. 2021).

The maximum winter ice thickness of water bodies in the study area rarely exceeds 2 m (Duguay et al. 2003; van Huissteden 2019) and maximally reaches 3 m according to local sources. The floating-ice lake of this study has a total surface area of  $0.51$  km<sup>2</sup> and reaches a maximum water depth of 6.9 m (Fig. 1, Supplementary Fig. S1a, b). It is mostly surrounded by peaty tundra shorelines towards the south and west but also borders a Late Pleistocene-aged yedoma plateau along its northwestern slope (Fig. 1) where yedoma is actively eroded (Supplementary Fig.

S1b). At the yedoma erosion site massive ground ice and yedoma deposits crop out at the surface. In the summer months blocks of yedoma soil and massive ground ice of several meters in diameter slump and slide into the floating-ice lake. The smaller bedfast-ice lake of this study is located 1.5 km north of the floating-ice lake, has a surface area of  $0.14$  km<sup>2</sup> and a maximum water depth of 2.8 m; thus, most of the lake is shallower than 2 m (Fig. 1, Supplementary Fig. S1c), thereby it classifies as a bedfast-ice lake.

In contrast, the bedfast-ice lake is exclusively surrounded by a low-lying and marshy tundra landscape with peaty soil. Both lakes are located in hydrologically closed depressions and are not connected to rivers or streams. The use of the terminologies bedfast- and floating-ice lake is no interpretive statement towards the sediment or carbon dynamics in the lakes, but simply scientific nomenclature.

### Sampling

In the summer of 2015 (14–19 July), lake depth measurements were taken with a Humminbird PiranhaMAX 160 fish finder and a Garmin GPS device (Fig. 1), bathymetry maps were created following Meisel et al. (2021). Along the shoreline of the floating-ice lake three soil samples were collected (Fig. 1; Table 1) from the tundra surface (S1, 0–5 cm depth) and the actively eroding yedoma permafrost cliff (S2 and S3, outcropping cliff face).

In the winter of 2016 (1–6 November), sediment cores were collected from both lakes with a UWITEC gravity corer from the frozen lake surfaces. Three sediment cores (F1–F3) were retrieved at the floating-ice lake. One sediment core (B1) was retrieved at the bedfast-ice lake (Fig. 1, Table 1). At each coring

**Table 1** Sampling details of sediment cores and shoreline samples

Location	Sample	Sampling date	Core length (cm)/material	Water depth (– m)/height above water level (+ m)	Long (°)	Lat (°)
Bedfast-ice lake	B1	4-nov-2016	69.5	– 1.7	147.40338	70.84802
Floating-ice lake	F1	5-nov-2016	77	– 3.1	147.41859	70.82973
	F2	5-nov-2016	113	– 6.5	147.42902	70.82953
	F3	3-nov-2016	86	– 3	147.43878	70.82980
	Shoreline sample 1	S1	16-jul-2015	Peat	+ 0.4	147.41468
Shoreline sample 2	S2	14-jul-2015	Yedoma	+ 10	147.44272	70.83085
Shoreline sample 3	S3	14-jul-2015	Yedoma	+ 1	147.44210	70.82915

site, a pair of two sediment cores was taken < 1.5 m apart. One core from each site was used for sediment sampling and the other for porewater extractions. After sample recovery, excess lake water was slowly drained from the PVC tubes above the collected sediment to preserve the sediment-water interface. At the sediment-water interface and the bottom the cores were carefully sealed with rubber caps and tape without trapping air pockets. The sediment cores were horizontally stored at 4–7 °C. Sediment porewater samples for DOC analyses were extracted and filtered (0.12–0.18 µm) in the field station within hours after sediment core collection at a 10 cm resolution with 5 cm long, hydrophilic, porous polymer MOM rhizons (Rhizosphere Research Products B.V.) and pre-evacuated vials following Meisel et al. (2021). The porewater samples were additionally treated with potassium iodide (KI) to prevent microbial activity.

The sediment cores and water samples were shipped at 4–7 °C to the laboratories of the Vrije Universiteit Amsterdam where they were stored dark and refrigerated at 4 °C. Due to cargo irregularities and resulting delays, the sediment cores could not be further processed until early 2018. During the transit period, the samples were kept dark and cooled.

### Core scanning analysis

At the Royal Netherlands Institute for Sea Research (NIOZ) the sediment cores were split open horizontally and XRF scanning at 10 and 30 kV was carried out with an XRF scanner (Avaatech Analytical X-Ray Technology) on the plain, open sediment surfaces (Hennekam et al. 2019). Amongst other elements, the cores were non-invasively scanned for silicon (Si), aluminum (Al), manganese (Mn) and iron (Fe) at a 1 cm resolution (counts/total counts). Additionally, linescan images were taken along the complete core profiles.

Measurements for MS and  $\rho_{\gamma\text{-ray}}$  were carried out at the sediment laboratory of the VU Amsterdam with a GEOTEK Multi-Sensor Core Logger (MSCL) at a 1 cm resolution. The non-invasive scanning results were calibrated against standardized objects of known magnetic properties and density.

### Sediment analysis

Analysis of the relative grainsize composition were carried out with a laser diffraction particle-sizer (Sympatec HELOS KR) at the sediment laboratory of the Vrije Universiteit Amsterdam. Prior to measurement, samples were pre-treated with 5 mL of 30% hydrogen peroxide (H<sub>2</sub>O<sub>2</sub>) and brought to boiling point to remove all OM. Subsequently, the samples were soaked in 5 mL of hydrochloric acid (HCl) to dissolve all carbonates and were again brought to boiling point with 300 mg of Na<sub>4</sub>O<sub>2</sub>P<sub>7</sub> to prevent particle conglomeration (van Buuren et al. 2020).

LOI data were obtained through thermogravimetric analysis (TGA) with a LECO TGA 701 at the sediment laboratory of the VU Amsterdam. The samples were heated in intervals at fixed rates up to 550 °C, while the weight loss through water evaporation and incineration of OM was recorded (van Buuren et al. 2020). The LOI data provided an estimate of the OM amount present in the analyzed sediment.

The porewater content was determined through the difference between wet and dry weights before and after sample drying for at least 48 h at 60 °C (Ackroyd 1957).

### OC analyses

The concentrations of DOC and their accompanying  $\delta^{13}\text{C}_{\text{DOC}}$  values were measured on the porewater samples. Flocculation of DOC was observed in some samples within days to weeks after collection. In order to quantify the total OC amount that was initially present as porewater DOC (and its  $\delta^{13}\text{C}$  signature) both, the dissolved carbon and the precipitated carbon had to be measured for carbon content and  $\delta^{13}\text{C}$  values following Meisel et al. (2021). The measurement results of the precipitated carbon and the DOC were joined as mass-based averages in order to determine the amount of DOC and its  $\delta^{13}\text{C}_{\text{DOC}}$  signature that was present in the porewater prior to flocculation.

The flocculates and the porewater samples were separated by filtering with combusted 0.7 µm GF/F filters. The filters were dried and placed into silver capsules with 25 µL of Milli-Q water and 25 µL of 1 M HCl for 30 min to remove any inorganic carbon compounds. An additional amount of 50 µL of 1 M HCl was added for 30 min; afterwards the samples

were dried at 60 °C for 3 h. The filters with the remaining precipitates were combusted and measured for their carbon amounts with a Carlo Erba NC 2500 elemental analyzer. The  $\delta^{13}\text{C}$  signatures were measured on a Thermo Finnigan Delta Plus isotope-ratio mass spectrometer (IRMS) coupled to the elemental analyzer. The  $\delta^{13}\text{C}$  measurements were calibrated against internationally recognized standards relative to Vienna Pee Dee Belemnite (VPDB); USGS24 ( $-16.05 \pm 0.07\%$  VPDB), USGS40 ( $-26.24 \pm 0.04\%$  VPDB), USGS41 ( $+37.76 \pm 0.05\%$  VPDB) and IAEA-CH-7 ( $-32.15 \pm 0.05\%$  VPDB) (Coplen 1996; Qi et al. 2003). Additionally, two in-house standards of glutamic acid ( $-24.08\%$ ) and birch leaf ( $-27.74\%$ ) were used. The analyses were carried out at the Systems Ecology laboratory at the Vrije Universiteit Amsterdam.

The DOC and  $\delta^{13}\text{C}_{\text{DOC}}$  analyses of the sediment porewater were carried out at the laboratory of the KU Leuven in Belgium with an Aurora 1030 W TOC carbon analyzer (OI Analytical) coupled to a Thermo Delta V Advantage IRMS (Meisel et al. 2021; Morana et al. 2015).

Briefly dissolved inorganic carbon was first removed by adding 10%  $\text{H}_3\text{PO}_4$  and stripping with He as carrier gas. Afterwards DOC was oxidized by adding 5% sodium persulfate ( $\text{Na}_2\text{O}_2\text{S}_8$ ) in a reaction at 97 °C for 10 min. The resulting  $\text{CO}_2$  was transferred to the IRMS after cryofocussing in a liquid  $\text{N}_2$  trap. The measurements were calibrated against two isotope standards at different carbon concentrations (IAEA-CH-6,  $-10.449 \pm 0.033\%$  VPDB and an in-house sucrose standard  $-26.99\%$ ).

The  $\delta^{13}\text{C}_{\text{org}}$  analyses were carried out with a FlashEA 1112 NC series elemental analyzer coupled to a Thermo Finnigan DELTA<sup>plus</sup>XP IRMS. For the analysis, the sediment samples were weighted into silver capsules and desiccated with 37% HCl for 12 h. Prior to analysis the samples were wrapped into tin capsules. The  $\delta^{13}\text{C}_{\text{org}}$  measurements were calibrated against the internationally recognized standards USGS24 ( $-16.05 \pm 0.07\%$  VPDB), USGS40 ( $-26.24 \pm 0.04\%$  VPDB), and USGS41 ( $+37.76 \pm 0.05\%$  VPDB) (Coplen 1996; Qi et al. 2003). The analysis was carried out at the Stable Isotope Laboratory of the Vrije Universiteit Amsterdam.

## Radiocarbon dating

The sample preparation for the  $^{14}\text{C}$  measurement on bulk samples and macrofossil samples was carried out at the Organic Matter laboratory of the Vrije Universiteit Amsterdam. The macrofossil samples (brown moss leaves and stems) were picked under a microscope from sieved (63  $\mu\text{m}$ ) bulk sediment samples soaked in 5% sodium hydroxide (NaOH). The macrofossil samples were prepared with an acid-alkali-acid (AAA) treatment. They were successively soaked with 0.5 M HCl (1 h, 60 °C), Milli-Q water (three rinses), 0.1 M NaOH (1 h, 60 °C), Milli-Q water (three rinses), 0.5 M HCl (1 h, 60 °C) and Milli-Q water (three rinses). The bulk lake sediment and shoreline soil samples were desiccated with fuming HCl (37%) and NaOH (5%) in that order at 60 °C over a period of 3 days for each compound. Finally, the macrofossil and bulk samples were dried at 60 °C (24 h).

The  $^{14}\text{C}$  measurements were carried out at the Laboratory for Ion Beam Physics of the ETH Zürich, Switzerland. The bulk samples were directly combusted and measured on a gas-ion-source-equipped MICADAS accelerator mass spectrometer (AMS) (Wacker et al. 2013). The macrofossil samples were graphitized prior to a high-precision measurement with a AMS (Wacker et al. 2010). The three measured  $^{14}\text{C}$  ages for the macrofossils of core F2 were calibrated to years before present (cal yr BP) using IntCal20 (Reimer et al. 2020) and the program CALIB 8.1.0 which is based on Stuiver and Reimer (1993). The three measured  $^{14}\text{C}$  ages for the macrofossils of core B1 were calibrated to negative cal yr BP (post AD 1950) with the software CALIBomb (Reimer and Reimer 2022) using the Northern Hemisphere Zone 1 (NHZ1) data set (Reimer et al. 2004). This was done to make them better comparable to the other  $^{14}\text{C}$  ages which are also displayed in cal yr BP. Bulk sample  $^{14}\text{C}$  ages were not calibrated due to their extensive mixing of different  $^{14}\text{C}$  sources.

## DNA extraction and analysis

A total of 72 sediment samples of circa 200 mg each were aseptically taken from the sediment cores at a 5 cm resolution. Before sampling, the top 1 mm of the exposed sediment surface was removed to avoid cross-contamination. After storage of the samples

at  $-20\text{ }^{\circ}\text{C}$ , DNA extraction was performed with the PowerSoil kit (Qiagen, Hilden, Germany) according to the instructions of the manufacturer at the Department of Ecological Sciences of the Vrije Universiteit Amsterdam. The 16S rRNA gene amplicon sequencing was carried out by Macrogen Inc. (Seoul, South Korea). In short, for bacterial diversity the V3–V4 region of the 16S rRNA gene was amplified by a 25 cycle PCR using universal bacterial primers Bac341F (5'-CCTACGGGNGGCWGCAG-3') and Bac785R (5'-GACTACHVGGGTATCTAATC-3'). For the amplification of archaeal sequences the same PCR settings were used with the primers Archf349 (5'-GYGCASCAGKCGMGAAW-3') and Archr789 (5'-GGACTACVSGGGTATCTAAT-3') (Klindworth et al. 2013). PCR clean ups, index PCR, adapter ligation and library preparation were done following the 16S rRNA gene Metagenomic Sequencing Library Preparation Part #15044223 Rev. B. The amplicon sequences were sequenced on the MiSeq V2-300cycle sequencing platform generating 7,639,276 archaeal reads and 4,235,199 bacterial reads in total. The QIIME2 (version 2019.7) platform was used for bioinformatic analysis. Demultiplexed bacterial sequences were first trimmed 270 bp on the forward read and 250 bp on the reverse reads, while archaeal sequences were trimmed on the forward and reverse reads to 270 and 230 bp, respectively. DADA2 was used for dereplication of the sequences with using default settings and chimera removal using the consensus mode. Amplicon sequence variants (ASV) were then aligned using MAFFT (Kato and Standley 2013) and phylogenetic distances were calculated with FastTree (Price et al. 2009). Taxonomic classification of the reads based on the SILVA v128 16S SSU NR database (Yilmaz et al. 2014) using QIIME 2's scikit-learn naive Bayes machine-learning classifier (Bokulich et al. 2018). At last, ASVs were removed that matched to mitochondrial or chloroplast sequences (Kato and Standley 2013) and phylogenetic distances were calculated with FastTree (Price et al. 2009). Processing of the microbial composition data was done using phyloseq v1.32 (McMurdie and Holmes 2013). We calculated the Shannon index for each sample and used non-metric multidimensional scaling (NMDS) on the Bray–Curtis dissimilarity measures between samples using the R-package 'vegan' v2.5 (Oksanen et al. 2022). We used the graphical function 'envfit' to describe correlations

between microbial community composition and environmental variables. NMDS analysis is a commonly used statistical approach in environmental community analysis (de Jong et al. 2018; Colby et al. 2020). The main reasons to use NMDS analysis were (i) to compare the composition of the sampled microbial communities and (ii) to test which environmental factors correlate with the observed differences in microbial community composition.

## Results

### Core descriptions

The sediments of the two lakes noticeably differed visually: while the floating-ice lake cores showed layering, the bedfast-ice lake had very homogenous and dark-brown sediment colors reflecting a high abundance of organic material. The floating-ice lake cores F1 and F3 both showed sporadic and indistinct layering due to variations in SOM content and had dark grayish brown, grayish brown and olive brown colors (Fig. 2) based on the Munsell Soil Color Chart (2009). Core F2 was strongly layered and had clear, distinct boundaries with layer thicknesses from a few mm up to 2 cm, the layering was most prominent between 60 and 16 cm depth (Fig. 2). The sediment colors ranged from grayish brown, dark grayish brown, dark brown, very dark brown to black based on the Munsell Soil Color Chart (2009). The top 16 cm of core F2 were especially rich in organic material and visible plant remains. The lower half of the core (111–60 cm) was considerably more homogeneous and lacked the distinct layering of the upper 60 cm.

Core B1 contained two main sediment facies (Fig. 2): (i) a very homogenous, unstratified, organic-rich, dark brown lake sediment at the top (36–0 cm) and bottom (69–59 cm) of the core and (ii) a gray, homogeneous deposit (59–36 cm) with sharp layer boundaries and strong color contrast to the brown lake sediment above and below. The lake sediment of core B1 was considerably more homogenous and of darker brown than the sediments of the cores F1–F3 from the floating-ice lake.

Plant remains (unidentified branches, strongly broken apart plant residues, plant roots, parts of *Betula nana*, brown mosses, *Sphagnum* spp.) as well as small shell fragments of bivalves and freshwater



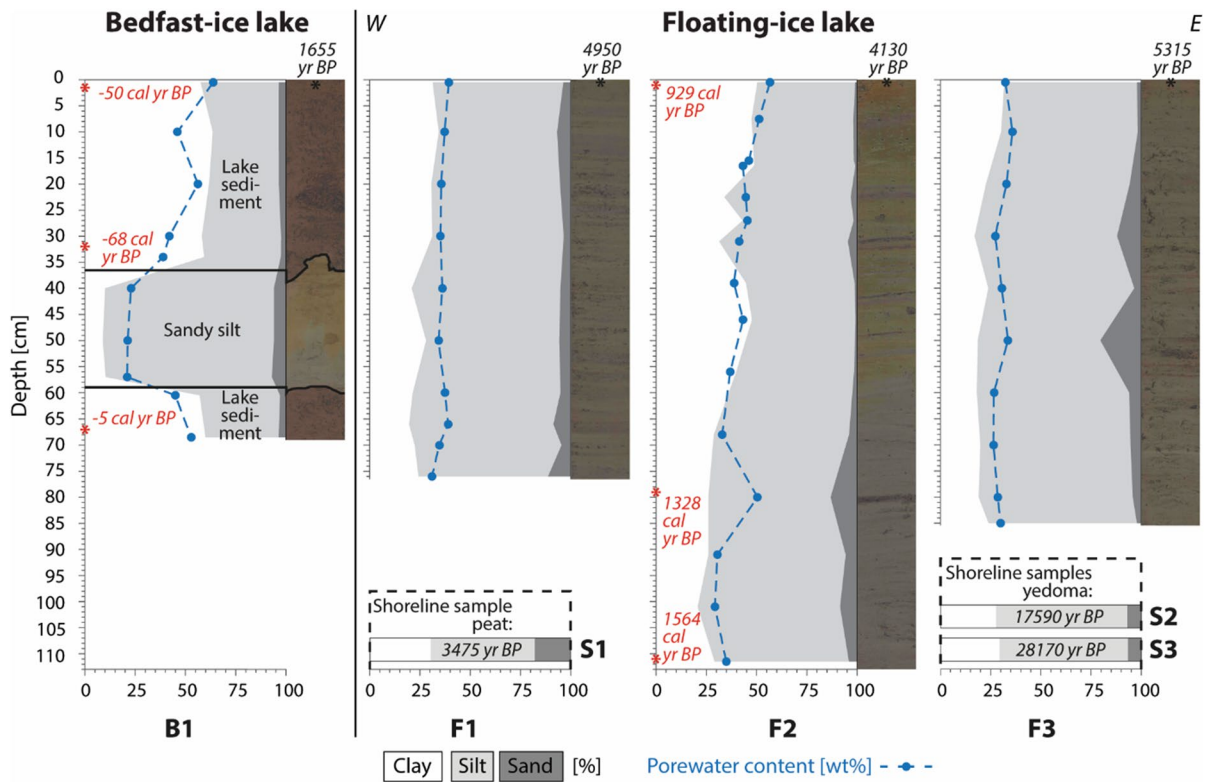


**Fig. 2** Plots of sediment cores B1 and F1–F3 display grain size distribution (clay, silt, sand), rounded average calibrated radiocarbon (<sup>14</sup>C) macrofossil ages (left side of core profiles B1 and F2), bulk sediment <sup>14</sup>C ages (at all core tops), porewater con-

tent (dashed and dotted line) and linescan photo images of the sediment cores. The grain size composition and bulk <sup>14</sup>C ages of the shoreline samples S1 and S2–S3 are displayed at the bottoms of the core profiles F1 and F3, respectively

ostracods were found throughout all cores in varying abundances.

**Physiochemical sediment properties**

The sedimentological and physical analysis showed that mineral components in the lake sediments were generally more abundant in the floating-ice lake while a separate pocket of particularly mineral-rich material was also found in the bedfast-ice lake (Fig. 2). Core F2, from the deepest part of the floating-ice lake, recorded with 38% the highest average clay content in the floating-ice lake compared to the cores F1 (26%) and F3 (23%). The clay content within the F2 core profile more than doubled from the bottom (21%, 101 cm) to the top (50%, 0.5 cm) while elevated sand contents were only found in the lower core section. The shoreline samples (S1–S3) had low clay contents around 30%.

Within the floating-ice lake, the average silt content was lowest at core site F2 (59%). With proximity to the shorelines at core sites F1 (68%) and F3 (71%) silt contents increased. Average sand contents were below 7% across the three floating-ice lake cores. This corresponded with the sand content of 7% at the yedoma plateau shoreline samples S2 and S3. The high sand content of 18% (S1) at the peaty western shoreline was not reflected in the nearby sediment core site F1. However, the high sand content at shoreline site S1 was likely due to the general methodology of the grain size measurement. For all grain size analyses the organic material was stripped from the sample and only the remaining mineral components were analyzed. If the high abundance of organic material would have been taken into account, too, the relative abundance of the sand component at site S1 would have been considerably lower.

In core B1 of the bedfast-ice lake the lake sediment (36–0 cm and 69–59 cm) had an average clay content of 60% compared to the average floating-ice lake clay content of 30% (F1–F3). The average silt (37%) and sand contents (3%) in the lake sediment of core B1 were lower than the averages of the floating-ice lake with 65% and 5%, respectively. The pocket with the homogenous deposit (59–36 cm depth) in core B1 was dominated by silt (84%) with low contents in sand (6%) and clay (10%).

The average sediment porewater contents of the floating-ice lake cores F1 (36 wt%), F2 (42 wt%) and F3 (30 wt%) were in a similar range. The average porewater content in the lake sediment of core B1 from the bedfast-ice lake was noticeably higher (49 wt%). The sandy silt pocket in core B1 (59–39 cm) contained the least amount of porewater with an average of 22 wt%.

The average sediment density ( $1.6 \text{ g cm}^{-3}$ ) and MS ( $9 \text{ cm}^3 \text{ g}^{-1}$ ) were higher in the floating-ice lake than in the lake sediment of the bedfast-ice lake core B1 with

$1.3 \text{ g cm}^{-3}$  and  $8 \text{ cm}^3 \text{ g}^{-1}$ , respectively. The sandy silt pocket of core B1 (59–39 cm) was also distinguishable from the surrounding lake sediment by its higher average sediment density of  $1.9 \text{ g cm}^{-3}$  (Fig. 3).

The Si/Al and Mn/Fe ratios of all four sediment cores had low, stable downcore values with two main exceptions (Fig. 3). Firstly, the sandy silt pocket in core B1 of the bedfast-ice lake had a considerably higher Si/Al ratio with an average value of 14 in comparison to the surrounding core B1 lake sediment with an average value of 8. Secondly, there was a strong difference in the Mn/Fe ratio within core F2, the lower core half (110–57 cm) had an average value of 0.02 while the top half (57–0 cm) had a significantly higher average value of 0.14.

#### Sedimentary and dissolved organic matter

SOM content and porewater DOC concentrations were higher in the bedfast-ice lake in comparison to the floating-ice lake. The shoreline samples from the

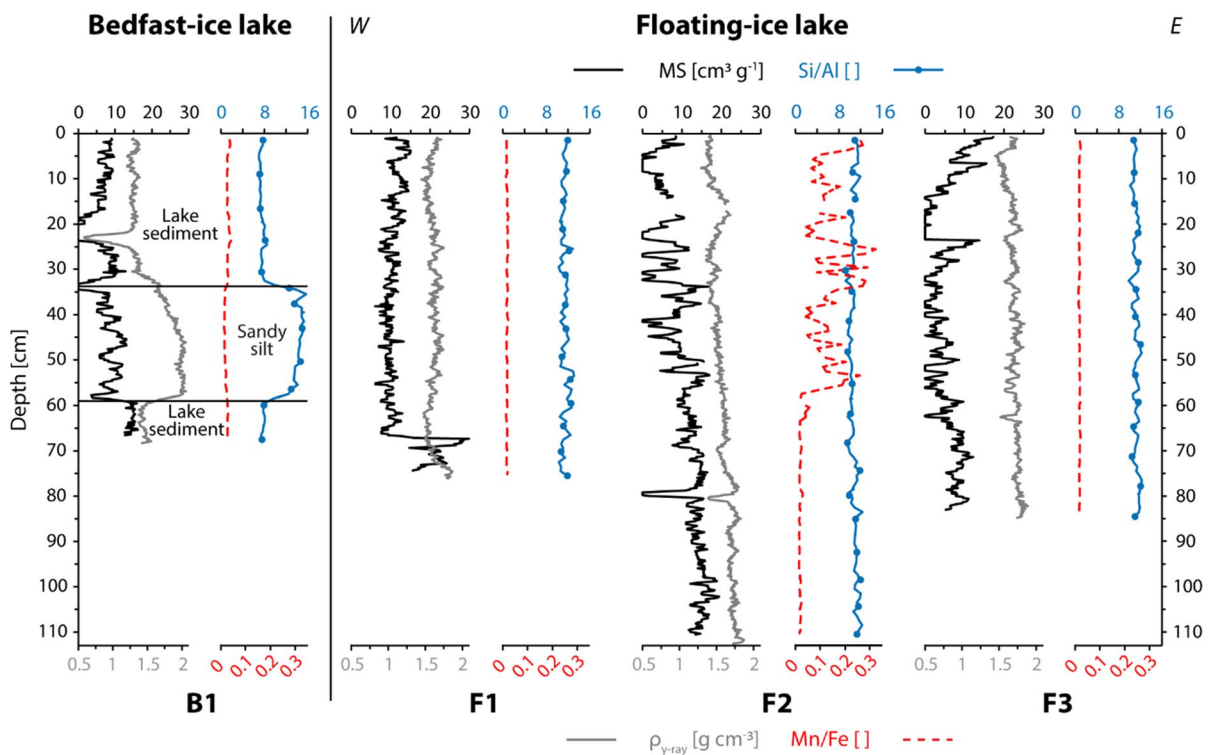


**Fig. 3** Physical property plots for the cores B1 and F1–F3 display profiles of magnetic susceptibility (MS; solid dark line), gamma-ray density ( $\rho_{\gamma\text{-ray}}$ ; solid light line), manganese/iron

ratio (Mn/Fe; dashed line) and silicon/aluminum ratio (Si/Al; solid, dotted line) based on XRF analyses

floating-ice lake significantly varied in their LOI values. Sample S1 from the peaty, western shoreline was almost entirely made up of OM with a LOI value of 73.3 wt% while the samples from the eastern shoreline with the eroding yedoma plateau (S2 and S3) were both below 6 wt%. The low OM content at the yedoma permafrost cliff was also reflected in the LOI values of the sediment cores F1–F3 of the floating-ice lake with an average LOI for each core below 8 wt% (Fig. 4).

The lake sediment of core B1 from the bedfast-ice lake had a considerably higher average LOI value

with 28 wt% while the sandy silt pocket of core B1 had an average of only 3 wt%. The differing amounts of SOM in the two different lakes were even stronger pronounced in the sediment porewater DOC concentrations. The combined average porewater DOC concentration across all three floating-ice lake cores (F1–F3) was  $56 \text{ mg L}^{-1}$  while the lake sediment of core B1 (35–5 cm) had an average of  $220 \text{ mg L}^{-1}$  (Fig. 4). No or insufficient amounts of porewater were extracted from the sandy silt pocket of Core B1. In all four cores DOC concentrations increased with sediment depth.

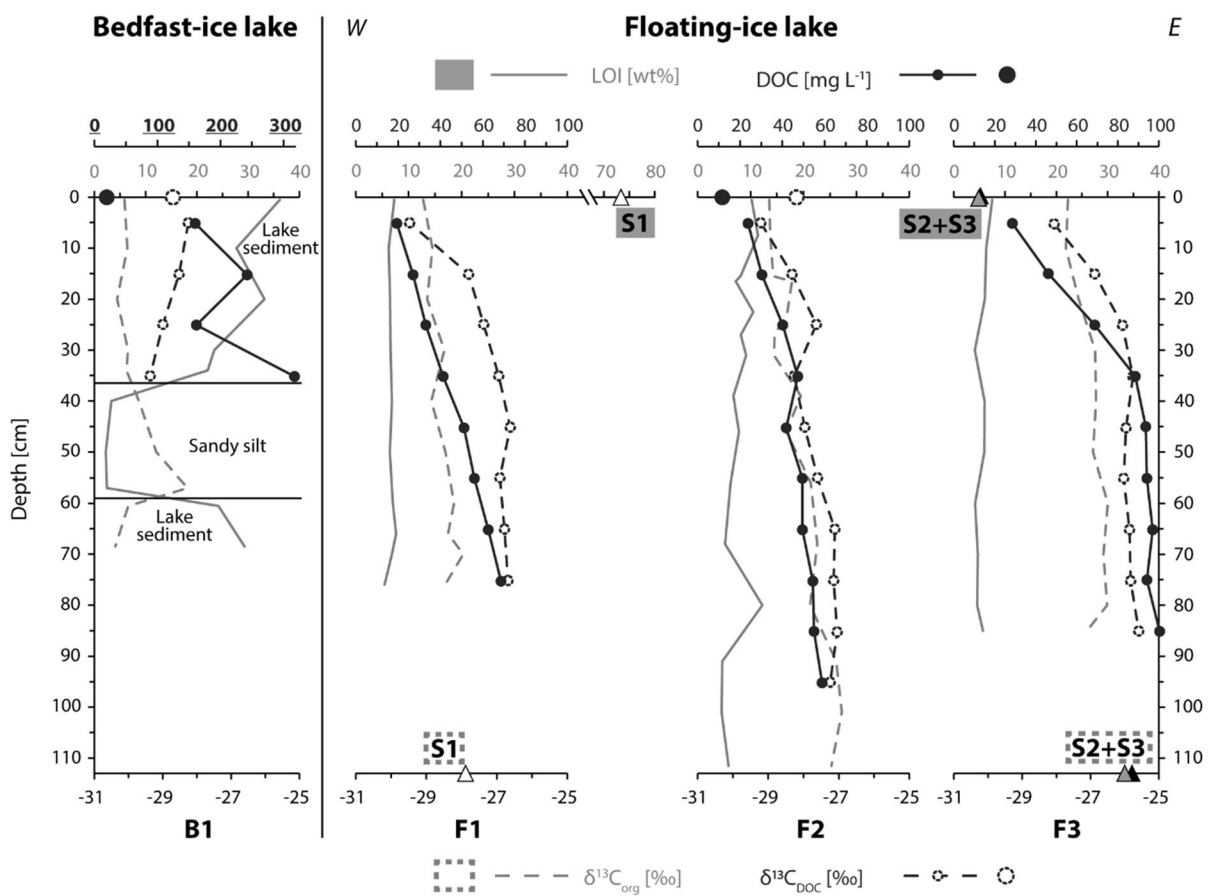


**Fig. 4** Carbon plots of the sediment cores B1 and F1–F3 show profiles for the loss-on-ignition (LOI; light and solid line), porewater dissolved organic carbon (DOC) concentrations (dark, solid and dotted line) and stable carbon isotope profiles of the DOC ( $\delta^{13}\text{C}_{\text{DOC}}$ ; dark, dashed and dotted line) and the soil organic carbon ( $\delta^{13}\text{C}_{\text{org}}$ ; light and dashed line). These data are also displayed for the three shoreline samples S1 and S2–S3 in the geographically nearest sediment core profiles of core F1 and F3, respectively (see Fig. 1). DOC concentrations

(filled circle) and  $\delta^{13}\text{C}_{\text{DOC}}$  values (dashed circle) of lake water samples are displayed at the top of core B1 and F2, respectively. The axes for DOC concentrations at the bedfast-ice lake (max.  $320 \text{ mg L}^{-1}$ ) and the cores in the floating-ice lake (max.  $100 \text{ mg L}^{-1}$ ) cover different ranges due to strong differences in DOC values. The LOI axis of core F1 is extended and interrupted to incorporate the high LOI value of shoreline sample S1

## Stable carbon isotope ratios of DOC and SOC in lake sediments

The  $\delta^{13}\text{C}_{\text{org}}$  values across the three cores of the floating-ice lake followed a general pattern from high values at the core bottom towards lower values at the core top (Fig. 4). The shoreline samples also differed strongly in their  $\delta^{13}\text{C}_{\text{org}}$  values from each other. Sample S1 from the peaty, western shoreline had the lowest  $\delta^{13}\text{C}_{\text{org}}$  value with  $-27.9\text{‰}$ , while the two shoreline samples S2 and S3 from the yedoma permafrost cliff had higher values of  $-26.0$  and  $-25.8\text{‰}$ , respectively. The difference in  $\delta^{13}\text{C}_{\text{org}}$  signatures between the shoreline samples S1 (peaty, west) and S2–S3 (yedoma, east) near the floating-ice lake was also reflected in the  $\delta^{13}\text{C}_{\text{org}}$  values of the three sediment cores with proximity (lower values) and distance (higher values) to the different shorelines. Within the floating-ice lake core F1 had the lowest average  $\delta^{13}\text{C}_{\text{org}}$  value ( $-28.6\text{‰}$ ), core F2 had an average value of  $-28.2\text{‰}$  and core F3 had the highest average  $\delta^{13}\text{C}_{\text{org}}$  value with  $-27.0\text{‰}$ . The average  $\delta^{13}\text{C}_{\text{org}}$  value in the lake sediment of core

B1 from the bedfast-ice lake was considerably lower with  $-30.1\text{‰}$  in comparison to the combined average  $\delta^{13}\text{C}_{\text{org}}$  value of the cores F1–F3 ( $-27.9\text{‰}$ ). The sandy silt pocket of core B1 had an average  $\delta^{13}\text{C}_{\text{org}}$  value of  $-29.1\text{‰}$  (Fig. 4).

The porewater  $\delta^{13}\text{C}_{\text{DOC}}$  profiles of the three cores in the floating-ice lake generally followed the same trend as the  $\delta^{13}\text{C}_{\text{org}}$  profiles with high values at the core bottom and low values at the core top. The highest average porewater  $\delta^{13}\text{C}_{\text{DOC}}$  value was detected in core F3 with  $-26.3\text{‰}$ , core F1 had an average of  $-28.6\text{‰}$  and core F2 had the lowest average with  $-27.7\text{‰}$ . The average porewater  $\delta^{13}\text{C}_{\text{DOC}}$  value in the lake sediment of core B1 was  $-28.8\text{‰}$ , this was considerably lower than the combined floating-ice lake  $\delta^{13}\text{C}_{\text{DOC}}$  average of  $-27.1\text{‰}$ . Additionally,  $\delta^{13}\text{C}_{\text{DOC}}$  lake water samples were analyzed for coring site F2 with  $-28.2\text{‰}$  and coring site B1 with  $-29.3\text{‰}$  (Fig. 4). Generally, higher SOM abundance appeared to correlate with higher DOC concentrations (Fig. 5a). Similarly, a direct relationship of higher  $\delta^{13}\text{C}_{\text{DOC}}$  values with elevated  $\delta^{13}\text{C}_{\text{org}}$  values was also observed (Fig. 5b).

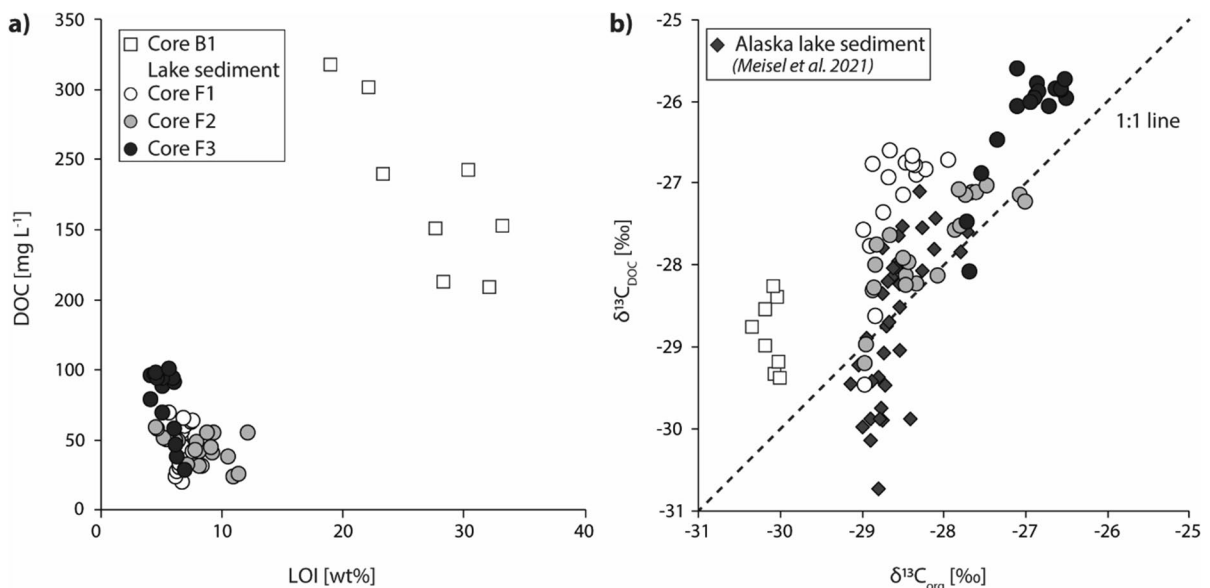


**Fig. 5** Linear interpolations were used in between data points to create matching data pairs at certain sediment core depths. **a** Dissolved organic carbon (DOC) and loss-on-ignition (LOI) data of the cores F1–F3 (circles) and the lake sediment of core B1 (boxes) are plotted against each other. **b** The ratios of the stable carbon isotope signatures for SOC (sediment organic

carbon) and DOC ( $\delta^{13}\text{C}_{\text{org}}$  and  $\delta^{13}\text{C}_{\text{DOC}}$ ) of the cores F1–F3 and the lake sediment of core B1 are displayed. Additionally,  $\delta^{13}\text{C}_{\text{DOC}}$  and  $\delta^{13}\text{C}_{\text{org}}$  data of Alaskan (Utqiagvik) floating-ice lake sediment (Meisel et al. 2021) are displayed for comparison (diamond icons)

The value ranges of  $\delta^{13}\text{C}_{\text{org}}$  and  $\delta^{13}\text{C}_{\text{DOC}}$  in the floating-ice lake developed mostly independent of SOM (LOI) abundances and DOC concentrations (Fig. 6a, b). The opposite trend was observed in the bedfast-ice lake where a larger variability in SOM (LOI) and DOC values did not appear to impact the value range of  $\delta^{13}\text{C}_{\text{org}}$  and  $\delta^{13}\text{C}_{\text{DOC}}$  (Fig. 6a, b).

### Radiocarbon ages of lake sediments

The most noticeable difference between the two lakes was the presence of young SOC in the bedfast-ice lake sediment, while the floating-ice lake sediment was dominated by considerably older SOC (Fig. 2; Table 2). The youngest bulk  $^{14}\text{C}$  age from the lakes was recorded at the top of sediment core B1 in the bedfast-ice lake with  $1655 \pm 60$  yr BP, while the bulk average  $^{14}\text{C}$  age from the three core tops of the floating-ice lake cores was much older at  $4800 \pm 490$  yr BP ( $1\sigma$ ,  $n=3$ ).

Furthermore, two macrofossil  $^{14}\text{C}$  age profiles were collected from the cores F2 and B1 for comparison of the lake ages. Core F2 had a chronological macrofossil  $^{14}\text{C}$  age profile from the bottom to the top with age ranges of 1611–1516 cal yr BP (111 cm), 1356–1300 cal yr BP (79 cm) and 956–902 cal yr BP (1 cm). The macrofossil  $^{14}\text{C}$  age profile of core B1 from the bedfast-ice lake contained contemporary

carbon, the yielded  $^{14}\text{C}$  ages and age ranges were of modern origin (post AD 1950) with  $-5$  cal yr BP (67 cm),  $-67$  to  $-69$  cal yr BP (32 cm) and  $-50$  to  $-51$  cal yr BP (1.5 cm).

The bulk shoreline sample S1 from the peaty western shoreline of the floating-ice lake yielded a  $^{14}\text{C}$  age of  $3475 \pm 70$  yr BP. The two bulk samples S2 and S3 from the yedoma permafrost cliff along the eastern shoreline of the same lake resulted in significantly older  $^{14}\text{C}$  ages of  $17590 \pm 130$  yr BP and  $28170 \pm 290$  yr BP, respectively.

### Microbial diversity of two contrasting lakes

The NMDS of community distance matrices showed that the bacterial and archaeal community compositions clearly differed between the two lakes (Fig. 7).

The bacterial community composition was most influenced by Mg ( $r^2=0.58$ ), water depth ( $r^2=0.56$ ), Al ( $r^2=0.52$ ), and Cr ( $r^2=0.42$ ) (Fig. 7, Supplementary Table S1). The environmental parameters with the strongest correlation for the archaeal community composition were Cl ( $r^2=0.46$ ), Mg ( $r^2=0.45$ ), Rh ( $r^2=0.45$ ) and Al ( $r^2=0.42$ ) (Fig. 7, Supplementary Table S1). Overall, water depth and elemental composition appeared as the strongest factors for inter-lake microbial community diversity. It is noteworthy, that the sediment depth also appeared to strongly impact

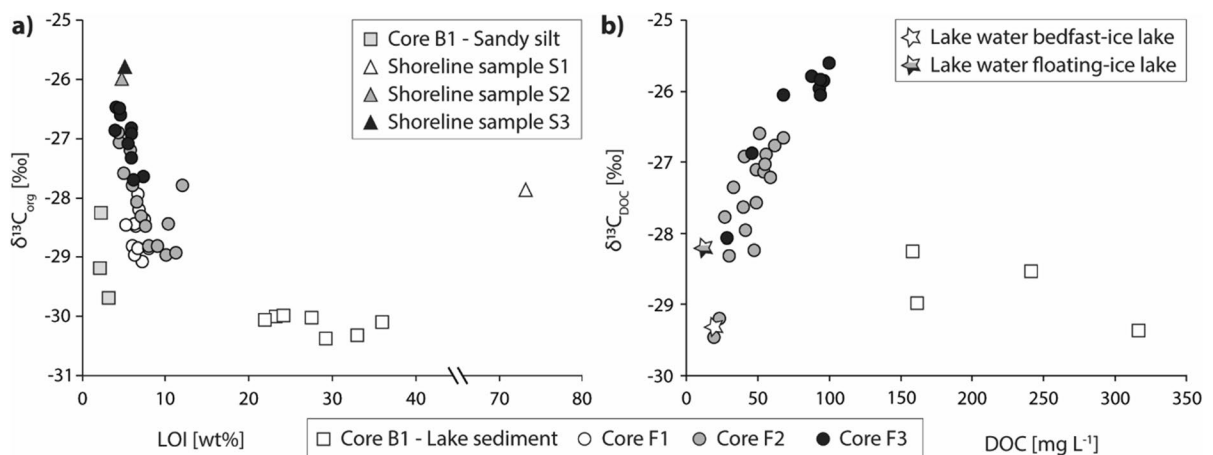


**Fig. 6** Linear interpolations were used in between data points to create matching data pairs at certain sediment core depths. **a** Sediment and soil organic carbon (SOC, soil-OC) stable carbon isotope signatures ( $\delta^{13}\text{C}_{\text{org}}$ ) are plotted against loss-on-ignition (LOI) data for cores B1 (boxes), F1–F3 (circles) and

the shoreline samples S1–S3 (triangles). The horizontal LOI-axis is interrupted between 40–70 wt%. **b** Dissolved organic carbon (DOC) stable carbon isotope signatures ( $\delta^{13}\text{C}_{\text{DOC}}$ ) are plotted against DOC concentrations for the cores B1 (boxes), cores F1–F3 (circles) and two lake water samples (star icons)

**Table 2** Overview of the radiocarbon ( $^{14}\text{C}$ ) analyses of the sediment cores B1 and F1–F3 and the shoreline samples S1–S3.

Location	Sample name	Lab no. ETH-	Core depth (cm)	Material	$^{14}\text{C}$ age (yr BP)	Age uncertainty (yr)	Calibrated $^{14}\text{C}$ age, 2- $\sigma$ range (cal yr BP)
Bedfast-ice lake	B1	97289	1	Bulk sediment	1655	60	–
	B1	97302	1.5	Brown moss leaves and stems	– 725	20	– 50 to – 51
	B1	97305	32	Brown moss leaves and stems	– 115	20	– 67 to –69
	B1	97303	67	Brown moss leaves and stems	– 5	20	– 5
Floating-ice lake	F1	97291	0.5	Bulk sediment	4950	70	–
	F2	97290	0.5	Bulk sediment	4130	70	–
	F3	97292	0.5	Bulk sediment	5315	80	–
	F2	97300	1	Brown moss leaves and stems	1000	20	956 to 902
	F2	97301	79	Brown moss leaves and stems	1440	20	1356 to 1300
	F2	97298	111	Brown moss leaves and stems	1665	25	1611 to 1516
Shoreline samples	S1	97295	(See Table 1 for sampling locations)	Bulk peat soil	3475	70	–
	S2	97294		Bulk yedoma soil	17590	130	–
	S3	97293		Bulk yedoma soil	28170	290	–

The three calibrated  $^{14}\text{C}$  age ranges of core F2 were calculated with IntCal20 (Reimer et al. 2020) while the negative calibrated age ranges of core B1 were calculated with the NHZ1 data set (Reimer et al. 2004)

the archaeal and bacterial community composition in the floating-ice lake (especially cores F1 and F2) as indicated by the elongated cluster shapes which successively follow the sampling depth (Fig. 7). These observations were also supported by noticeable differences in the Shannon Diversity Index in both, the archaeal and bacterial communities, of the two lakes (Supplementary Fig. S2).

The distribution of the different archaeal taxonomic levels of phylum (Supplementary Fig. S3), class (Supplementary Fig. S4), order (Supplementary Fig. S5), family (Supplementary Fig. S6), and genus (Fig. 8) are also displayed in more detail. In addition, the distribution of the anaerobic methane oxidizing archaeon *Candidatus* ‘Methanoperedens’ (Supplementary Fig. S7) is shown separately. The distribution of the bacterial taxonomic levels of phylum

(Supplementary Fig. S8), class (Supplementary Fig. S9), order (Supplementary Fig. S10), family (Supplementary Fig. S11) are also displayed in detail in the supplementary figures. In addition, the aerobic bacterial methane oxidizers of the Methylomonadaceae family (Supplementary Fig. S12) are shown separately.

We observed 1142 bacterial ASVs across all samples. The bacterial communities were dominated by Proteobacteria (44.0%), Bacteroidota (23.3%), Chloroflexi (5.9%), and Acidobacteriota (3.0%) across all sediment cores (Supplementary Fig. S8). In the three floating-ice lake sediment cores the most abundant bacterial orders were Burkholderiales (36.0%), Bacteroidales (13.0%), Sphingobacteriales (4.1%), Caulobacteriales (3.1%), Spirochaetales (3.0%), and Campylobacteriales (3.0%) while in the bedfast-ice

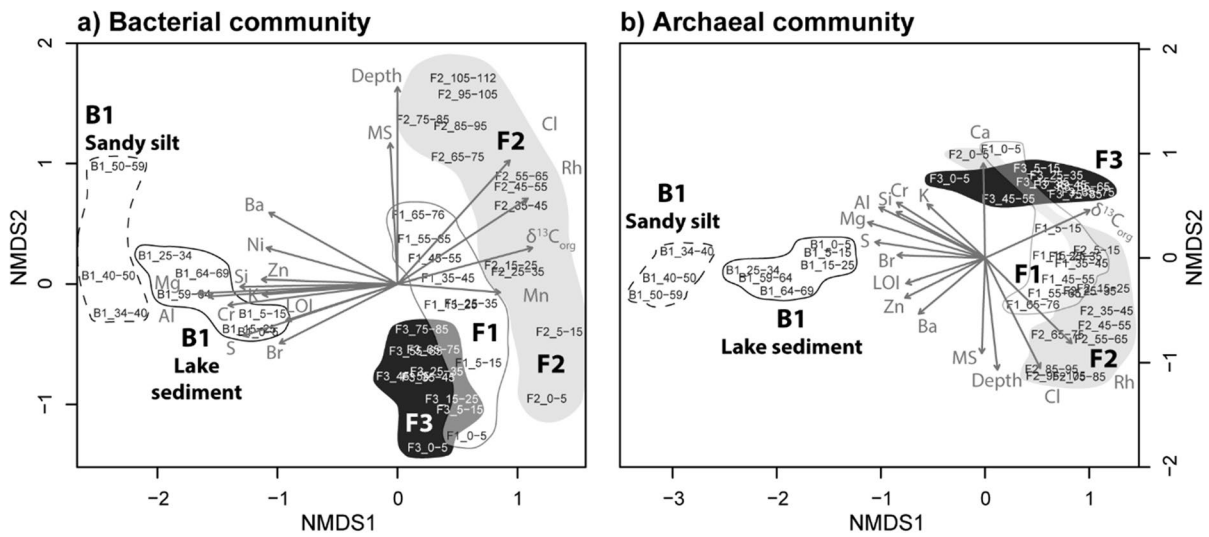


**Fig. 7** Non-metric multidimensional scaling (NMDS) plots of the microbial community diversities with clusters for the sediment cores F1 (no fill, light outline), F2 (light fill), F3 (dark fill), B1 Lake sediment (dark outline), B1 Sandy silt (light and dashed outline). The environmental parameters include the (XRF-based) elements Mg, Al, Si, S, Cl, K, Cr, Mg, Al, Si,

S, Cl, K, Cr, Zn, Rh, Ba as well as lake water depth (Depth), magnetic susceptibility (MS), loss-on-ignition (LOI) and  $\delta^{13}C_{org}$ . **a** The bacterial community plot additionally includes the (XRF-based) elements Mn and Ni as environmental parameters while **b** the archaeal plot additionally contains the (XRF-based) element Ca

lake the orders of Burkholderiales (31.5%), Bacteroidales (21.7%), Flavobacteriales (7.4%), Anaerolineales (4.9%), and Pseudomonadales (3.3%) were most dominant (Supplementary Fig. S10). We detected sequences of the aerobic methanotrophic genus *Methylobacter* of the Methylomonadaceae family in all sampled cores (Supplementary Figs. S11–12).

The archaeal community was dominated by Euryarchaeota (49.0%), Bathyarchaeota (26.7%), Woeisearchaeota (DHVEG-6) (14.4%), Thaumarchaeota (3.8%), and Altiarchaeales (1.3%) (Supplementary Fig. S3). However, the bedfast-ice lake samples showed a significant difference in their archaeal community composition compared to the floating-ice lake (envfit;  $P < 0.05$ , Figs. 7 and 8). We observed several methanogenic orders, including, Methanomicrobiales and Methanosarcinales (Supplementary Fig. S5). The abundance of these orders varied strongly, for example for Methanosarcinales, with 77.2% in core B1 at 50 cm depth (sandy silt), and 13.4% in sediment core F1 at 55 cm depth (Supplementary Fig. S5).

In both lakes, acetoclastic *Methanosaeta*, acetoclastic and methylotrophic *Methanosarcina* and hydrogenotrophic methanogens were observed in the methanogenic communities (Fig. 8). The methanogenic

communities of the bedfast-ice lake and floating-ice lake differed in the most abundant methanogenic genera.

In the bedfast-ice lake the methanogenic community was dominated by the hydrogenotrophic *Rice Cluster II*, *Methanosaeta*, *Methanosarcina* and *Methanobacterium*, while the cores from the floating-ice lake showed a dominance of *Methanoregula*, *Methanosaeta*, *Rice Cluster II* and *Methanomicrobiaceae* (Fig. 8).

In the bedfast-ice lake core B1, the archaeal community profiling also showed the presence of the anaerobic methanotrophic archaeon *Ca. 'Methanoperedens'* with varying relative abundances of 1.6% (0.5 cm, lake sediment) and 65.8% (50 cm, sandy silt) within the Euryarchaeota (Fig. 8, Supplementary Fig. S7). *Ca. 'Methanoperedens'* was also present in the top 10 cm of core F3, but especially in the top 30 cm of core F2 (Fig. 8 and S7). These archaea oxidize methane at the expense of nitrate, Fe(III) or Mn(IV) (Haroon et al. 2013; Cai et al. 2018; Leu et al. 2020); from the phylotype, however, it was not possible to deduce which substrate they used at this particular site. However, *Ca. 'Methanoperedens'* was mostly absent or present in low abundances ( $< 1\%$ ) in 48 out

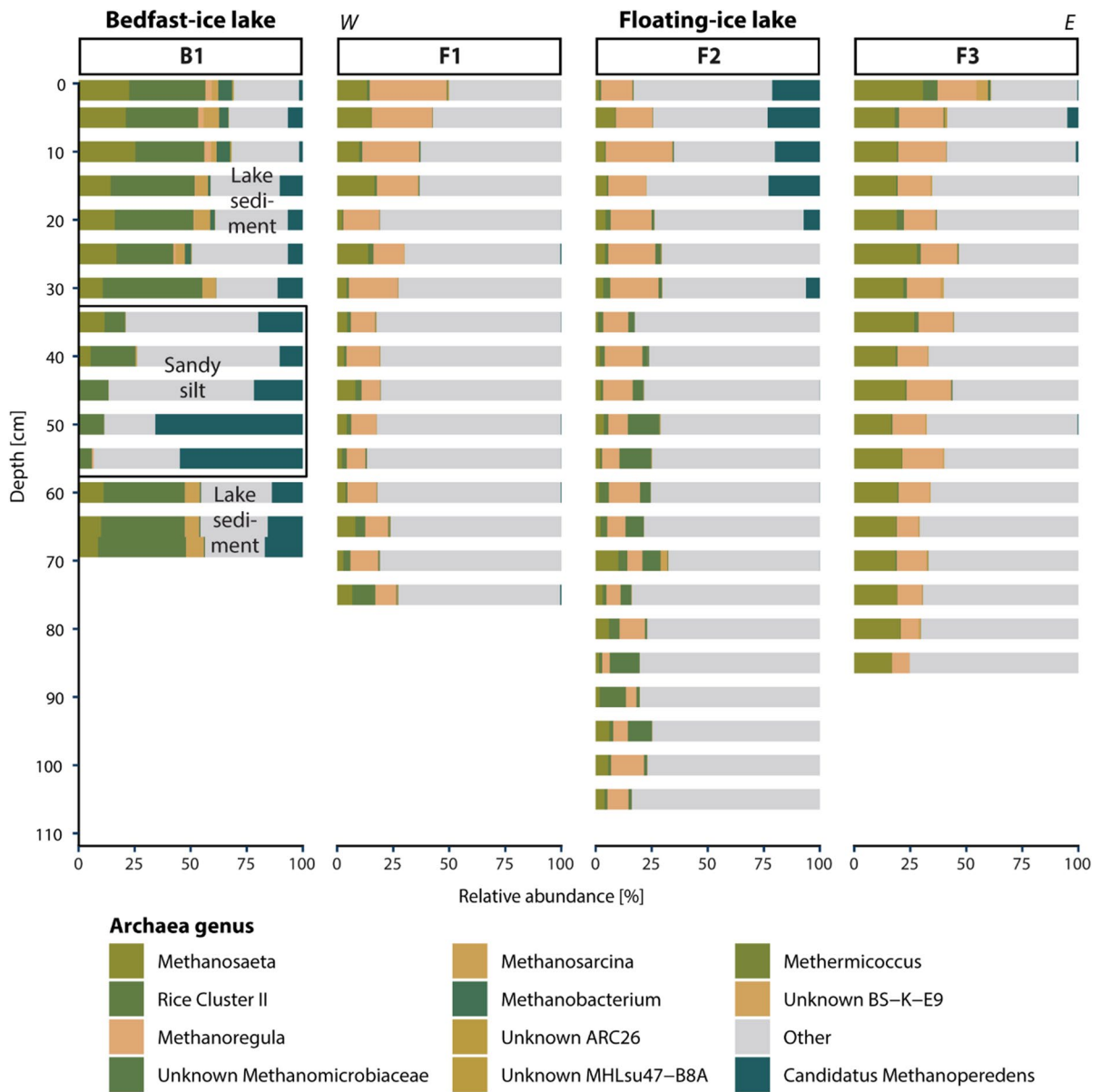


**Fig. 8** Diversity plot of relative archaea genus abundances in sediment cores B1 and F1–F3 with a colormap from Crameri (2021). ‘Unknown’ here indicates taxa that belong to undescribed genera within higher level orders of *Archaea*



of 56 floating-ice lake samples (Fig. 8 and S7). No other archaeal methanotrophs were found.

## Discussion

### Lake sediment dynamics

The visual sediment properties within the floating-ice lake (F1–F3) are variable due to different proximities of the individual coring sites to the shorelines (peaty vs. eroding yedoma permafrost cliff) and differing lake depths (Fig. 1). The biogeochemical properties in the sediments of the bedfast-ice lake (B1) and the floating-ice lake (F1–F3) additionally differ. Partially, this is likely due to the different environmental conditions and temperatures at the lakebeds due to the presence or absence of a talik.

One main difference in sedimentation between the core sites is the high average clay content at site F2 ( $37.8 \pm 9.8\%$ ,  $n = 15$ ) in comparison to the cores F1 ( $26.4 \pm 5.0\%$ ,  $n = 10$ ) and F3 ( $22.5 \pm 4.8\%$ ,  $n = 10$ ) within the floating-ice lake. This difference is likely due to an increased share of suspension-driven particle deposition at the deep core site F2 opposed to the transport of larger sediment particles through wave-induced motion that is naturally more pronounced at the shallower core sites F1 and F3 (Fig. 2). The suspension-driven sedimentation at coring site F2 is also a direct effect of the longer distance to the shorelines (Fig. 1). Over time, the floating-ice lake steadily grew through horizontal shoreline erosion and subsidence through vertical talik growth. At a certain critical water depth suspension-driven clay sedimentation became dominant at the F2 core site which is visible through an increased entry of the clay component and a decrease in sand particles from 60–0 cm depth (Fig. 2).

Ratios of Mn/Fe are widely used in lake studies as semi-quantitative proxies for past changes in redox and hypolimnic conditions (Simola 1983; Bouchard et al. 2011; Biskaborn et al. 2013) since both Mn and Fe are highly redox-sensitive (Davison 1993; Bouchard et al. 2011). Usually, the presence of Mn in lake sediments indicates well-oxygenated conditions of bottom waters and sediment surfaces (Davison 1993) where Mn-bearing minerals authigenically precipitate and accumulate (Bouchard et al. 2011). In contrast, the presence of Mn in core F2 (57–0 cm,

6.5 m water depth) might be an indication for seasonally hypolimnic conditions in winter near the deepest point (6.9 m) of the floating-ice lake (Fig. 3). Mn-bearing minerals at the lakebed would not be stable in stratified and hypolimnic conditions and dissolve in the absence of oxygen. A process called ‘geochemical focusing’ during which cold and heavy bottom water enriches in dissolved Mn at the deepest part of a lake with Mn from the shallower lake sections (Schaller and Wehrli 1996) could provide an explanation. During spring melt, ice breakup and incipient wave motion, oxygen is reintroduced to the bottom water and the dissolved Mn might precipitate as part of various compound minerals (Davison 1993; Scholtysik et al. 2020; Makri et al. 2021). With high sedimentation rates through shoreline erosion, such precipitated Mn-bearing minerals might be quickly buried in the lake sediment. Across all four sediment cores of this study, Mn was only detected in considerable amounts at this deepest part of the floating-ice lake at core site F2 (57–0 cm). This suggests that the Mn/Fe ratio may here be an indicator for at least seasonally anoxic conditions (Fig. 3), however, more data are needed to confirm this hypothesis.

Another interesting feature is the sandy silt pocket that was deposited in the bedfast-ice lake at coring site B1. Since the sandy silt pocket is under- and overlain by lake sediment, a significant physical force had to be present to put the coarse-grained deposit in place. Therefore, it can be assumed that it is of allochthonous origin. Possible explanations for its formation might range from sediment erosion and depositions through ice rafts, sudden lake drainage with erosion and redeposition through strong water currents (Jones and Arp 2015) or cryoturbation processes in the subsoil that pushed the silt deposit into its current position (Ballantyne 2018; French 1996). The origin of this sandy silt deposit is not the focus of this study and is therefore not discussed in further detail.

Si/Al ratios are generally used as indicators for changes in sediment sources over time. A higher value indicates an increase in the relative abundance of silica minerals like quartz ( $\text{SiO}_2$ ) which are of terrestrial origin (Aniceto et al. 2014; Ulrich et al. 2021) and usually a by-product of erosion processes. The grainsize distribution,  $\rho_{\gamma\text{-ray}}$  and Si/Al ratio (Fig. 3) all suggest an overall high and steady contribution of mineral, silica-bearing material (likely from the

eroding yedoma permafrost cliff) into the floating-ice lake sediment at all three core sites (F1–F3) in comparison to the bedfast-ice lake. The lake sediment of the bedfast-ice lake (B1) contains by comparison much less silica material indicated by a noticeably lower Si/Al ratio, overall lower density (Fig. 3) and lower sand and silt contents (Fig. 2). This observation does not take the sandy silt pocket of core B1 from the bedfast-ice lake into account since it is most likely of allochthonous origin.

#### Carbon age, origin and degradation in the thermokarst lake sediments

The eroding yedoma permafrost cliff (S2, S3) contains old OC of Late Pleistocene age that slumps into the floating-ice lake (Fig. 1). Similar Late Pleistocene  $^{14}\text{C}$  age ranges (20,829 to 31,745 cal yr BP) were measured by Weiss et al. (2015) along the same cliff. Consequently, considerably older SOC is present in the floating-ice lake sediments in comparison to the bedfast-ice lake sediments. This is reflected in both, the bulk and negative macrofossil  $^{14}\text{C}$  ages of core B1 (Fig. 2; Table 2). This observation is also supported by Dean et al. (2020) who studied  $^{14}\text{C}$  ages of DOC, particulate organic carbon, dissolved  $\text{CO}_2$  and dissolved  $\text{CH}_4$  from the same two lakes. The bedfast-ice lake appears to receive the bulk of its SOC from the surrounding peaty soils and tundra vegetation which contains mainly contemporary carbon, which is especially reflected in the negative (post AD 1950) macrofossil  $^{14}\text{C}$  ages (Fig. 2; Table 2). The strong differences between the macrofossil and bulk  $^{14}\text{C}$  ages from the tops of the cores B1 and F2 are also noteworthy. It shows that younger, contemporary and older, reworked carbon clearly stem from different sources, most likely from the peaty tundra soil and tundra vegetation (contemporary), and the yedoma cliff and other subsoils (old), respectively. Generally, the presence of old OC (to different degrees) at the top of all sediment cores, in both the macrofossil and bulk samples, is a representation of the continuous erosion of old carbon along the lake shorelines and its mixing and deposition in the lake sediments.

The  $\delta^{13}\text{C}_{\text{org}}$  and  $\delta^{13}\text{C}_{\text{DOC}}$  values of the bedfast-ice lake are considerably lower than in the floating-ice lake (Fig. 4), and their relationships with the corresponding carbon concentrations and abundances also differ between the two systems (Fig. 6a, b). The

concentration of porewater DOC in the sediment across all lakes was found to be strongly related to the amount of available SOM (Fig. 5a), with higher DOC concentrations for the bedfast-ice lake and lower for the floating-ice lake. Similarly, the sediment porewater  $\delta^{13}\text{C}_{\text{DOC}}$  values correlated positively to  $\delta^{13}\text{C}_{\text{org}}$  values of the lake sediments (Fig. 5b). The bedfast-ice lake has distinctly different sedimentary carbon characteristics with up to three times higher LOI values as well as DOC concentrations and considerably lower  $\delta^{13}\text{C}_{\text{DOC}}$  and  $\delta^{13}\text{C}_{\text{org}}$  values than the cores F1–F3 from the floating-ice lakes (Fig. 6a,b). Interestingly, the measured  $\delta^{13}\text{C}_{\text{org}}$  values of the cores F1 and F2 in the floating-ice lake are rarely lower than  $-29\%$ . A similar observation was also made for lake sediment  $\delta^{13}\text{C}_{\text{org}}$  values from two floating-ice lakes near Utqiagvik, Alaska (Meisel et al. 2021) (Fig. 5b). These similar  $\delta^{13}\text{C}_{\text{org}}$  values in both the Siberian and Alaskan samples might suggest, that the SOC at these core sites might have undergone a similar degree of degradation under similar floating-ice conditions. This observation is especially noteworthy, since the two Alaskan lakes are not bordering an actively eroding yedoma cliff with Pleistocene-aged OM but have a very similar setting to the Siberian bedfast-ice lake of this study in a flat tundra landscape with characteristic tundra vegetation. This might be an indication that the lake ice regime also plays an important role in how OM in thermokarst lakes is decomposed. Lake sediments in floating-ice lakes remain unfrozen year-round which facilitates OC degradation. Under these conditions the most easily degradable, volatile, and  $^{12}\text{C}$ -enriched OC components might be preferentially processed and removed while more  $^{13}\text{C}$ -enriched OC might remain in the sediment or porewater (Ågren et al. 1996). Bedfast-ice lakes, on the contrary, have frozen lakebeds in winter. This reduces the overall levels of OC degradation through a more limited time window for microbial activity due to lower soil and sediment temperatures in winter (Thornton et al. 2015; Wik et al. 2016), this might here be reflected in the lower  $\delta^{13}\text{C}_{\text{org}}$  value range of the core B1 lake sediment ( $-30.4$  to  $-30.0\%$ ).

The differences in  $\delta^{13}\text{C}_{\text{org}}$  and  $\delta^{13}\text{C}_{\text{DOC}}$  values between both lakes and within the floating-ice lake are certainly also influenced by their SOM origin, which is reflected in the  $\delta^{13}\text{C}_{\text{org}}$  range of the shoreline samples consisting of peat ( $-27.9\%$ ) or yedoma ( $-26.0\%$  and  $-25.8\%$ ). The lake

sediment of core B1 in the bedfast-ice lake has a low  $\delta^{13}\text{C}_{\text{org}}$  value range ( $-30.4$  to  $-30.0\text{‰}$ , range  $0.4\text{‰}$ ). This indicates a more homogenous OC source and limited fractionation by OM decomposition. On the contrary, the sediment cores of the floating-ice lake show greater  $\delta^{13}\text{C}_{\text{org}}$  variability ( $-29.1$  to  $-26.5\text{‰}$ , range  $2.6\text{‰}$ ) which may point towards the input of OC from different and heterogeneous sources. A complicating factor is that these different OC sources may already exhibit different degrees of carbon degradation prior to the secondary deposition as lake sediment. Weiss et al. (2015) found that, at the same Kytalyk field site, the soil-OM of the Late Pleistocene yedoma plateau (S2 and S3) has undergone considerably higher degrees of decomposition than the surrounding younger soil-OM of the peaty tundra landscape (S1) based on lower soil-OM contents, lower C:N ratios and higher  $\delta^{13}\text{C}_{\text{org}}$  values. Especially, deeper layers rich in OC, such as buried peat or cryoturbated layers, were relatively well preserved and undecomposed in comparison to the yedoma soils (Weiss et al. 2015).

In summary, the observed patterns in LOI, DOC,  $\delta^{13}\text{C}_{\text{org}}$  and  $\delta^{13}\text{C}_{\text{DOC}}$  in the lake sediments of our study can be explained by a combination of different sediment source inputs and varying intensity of (prior or in situ) degradation processes. These differences between the two lakes are summarized in the schematic overview of Fig. 9 which outlines how the different seasons, lake depths and shorelines impact the OC dynamics. Future studies of lake sediments at this field site would benefit from additional data like C:N ratios and molecular analyses to better differentiate the lake sediment composition with regard to potential aquatic primary production of OM in the lake systems and differences in SOM decomposition. To what extent primary production of OM within the lake contributed to the lake SOC pool was not quantified here. Aquatic production in thermokarst lakes can be significant with increases in nutrient supply (Bouchard et al. 2017) and offset the GHG release from the lake systems over millennial timescales (Walter Anthony et al. 2014). However, primary production of high latitude lakes is known to be low due to the cold

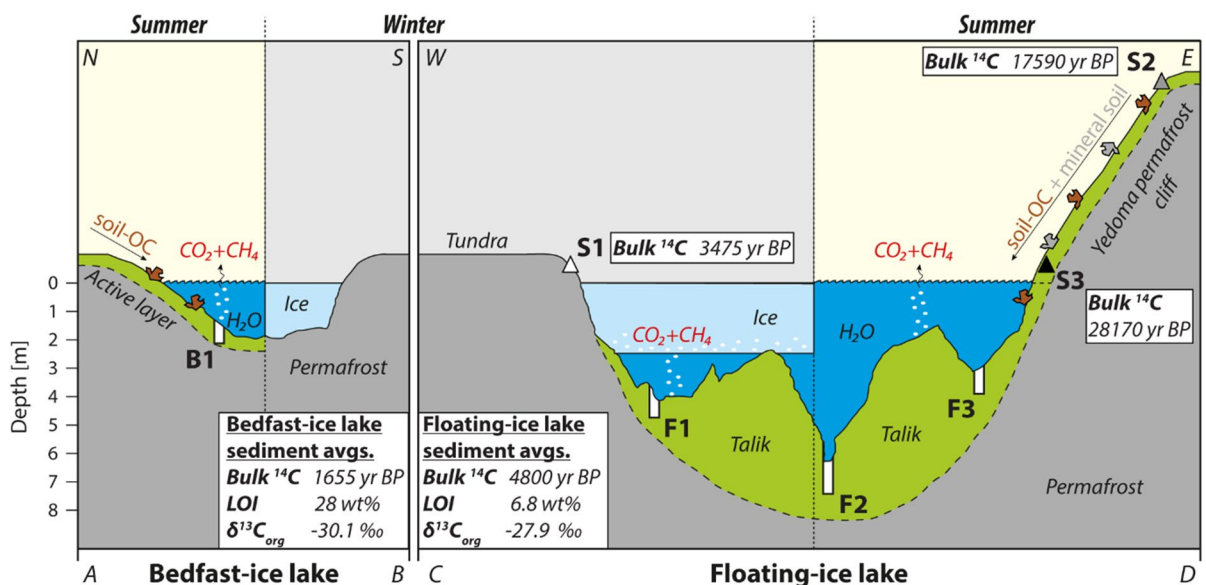


**Fig. 9** Schematic overview of field site for both lakes during summer and winter season. The lake bathymetry cross sections of both lakes are based on the original bathymetry maps in Fig. 1 (exported from QGIS) along the profiles A–B (bedfast-ice lake) and C–D (floating-ice lake). The lake widths, lake depths and sediment core lengths are displayed in correct scale and proportion relative to both lakes. Bulk  $^{14}\text{C}$  ages are displayed for all sediment core tops (F1–F3 average) and shore-

lines samples. Loss-on-ignition (LOI) and stable carbon isotope values of the soil organic carbon (soil-OC) and sediment organic carbon (SOC) ( $\delta^{13}\text{C}_{\text{org}}$ ) are displayed as averages for the lake sediment of the bedfast-ice lake (B1) and all cores of the floating-ice lake (F1–F3). The irregular-shaped icons along the lake shorelines in summer represent erosion of shoreline material into the lake

temperature conditions and short summer seasons (Shaver and Chapin 1991; Hinkel et al. 2003; Lenz et al. 2016) and is therefore unlikely to be a major contributor of OM to the lakebeds. Manasypov et al. (2022) also pointed out that OM input into thermokarst lakes in Western Siberia appeared to be dominated by allochthonous materials that were drowned below the lakebed and eroded along the shorelines.

#### Differences in microbial communities between two contrasting thermokarst lakes

The bedfast-ice and floating-ice lake show significant differences in their archaeal and bacterial community compositions. Based on the NMDS analysis both communities were significantly influenced by the differences in mineral sediment components (XRF), SOM content (LOI), OC sources ( $\delta^{13}\text{C}_{\text{org}}$ ), the lake type (water depth) and sediment depth (Fig. 7). The overarching factors that are most likely to explain the differences in lake sediment microbial community composition are the lake ice regime (i.e., temperature-driven) and the sediment source (i.e., nutrient-driven). Firstly, the lake ice regime determines the prevailing lake sediment temperature throughout the long winter season which is a main driver for sedimentary microbial activity (Wik et al. 2014; Thornton et al. 2015). In floating-ice lakes this is year-round above freezing temperatures, while in bedfast-ice lakes this is only above freezing temperatures in summer. Secondly, the varying sediment sources from eroding shorelines (peaty tundra soil vs. yedoma soil) act as the main nutrient and OM supplies (Fig. 9) and microbial growth is highly dependent on nutrient availability (de Jong et al. 2018). In this study we could, however, not quantify to which degree each of these factors impacted the microbial community composition.

It is also noticeable, that significant shifts in the composition of both, archaeal and bacterial communities appear to take place with increasing sediment depth within each individual core of the floating-ice lake, as displayed by the elongated core clusters (F1-F3) of the NMDS (Fig. 7). This might be an expression of the talik presence and the clearly stratified and heterogenous sediment layers, especially in cores F1 and F2. The same trend cannot be observed for the lake sediment of core B1 from the bedfast-ice lake. Here, a less pronounced down-core profile

in microbial community variability is observed, this might be due to the colder environmental conditions, which are here a more restricting factor for microbial growth in the overall more homogenous lake sediments (B1).

Because microbial activity data are not available for this study, any explanations for the observed differences in microbial community compositions between the two lakes remain to a certain degree speculative. However, as there are clear differences in the methanogenic and methanotrophic communities in the lakes, as well as the SOM content, it is likely that methane dynamics in each of the studied lakes are also different. While both lakes harbor archaea capable of acetoclastic and hydrogenotrophic methanogenesis, the genus of *Rice Cluster II* is more abundant in the bedfast-ice lake (Fig. 8). In contrast, *Methanoregula* is more abundant in the floating-ice lake (Fig. 8). Sediment incubations from Alaskan thermokarst lakes have indicated, that the abundance of *Rice Cluster II* and *Methanoregula* are often related to hydrogenotrophic and methylotrophic methanogenesis (de Jong et al. 2018). However, the presence of *Methanosaeta* and *Methanosarcina* could also indicate potential acetoclastic and methylotrophic methanogenesis (Fig. 8). The large diversity of methanogenic species in the two lakes of this study might support the potential capacity for aerobic methanotrophy by Type I methanotrophs, belonging to the family of Methylomonadaceae, and anaerobic methanotrophy by *Ca. Methanoperedens* species coupled to either nitrate, Fe(III) or Mn(IV) reduction in both lakes. Particularly, in the bedfast-ice lake sequences of the genus *Ca. Methanoperedens* were highly abundant. Within this genus, *Ca. Methanoperedens nitroreducens* is commonly observed in thermokarst lake sediments (Matheus Carnevali et al. 2018; de Jong et al. 2018; Kallistova et al. 2021) and has also been associated with high in situ anaerobic methane oxidation rates in sediments of thermokarst lakes (Winkel et al. 2019). Interestingly, the anaerobic methane oxidizers were less abundant in the floating-ice lake, which could indicate a loss of anaerobic methane oxidation under these warmer conditions (Fig. 8). Further studies (incubations, microbial activity, nutrient availability) comparing the different lake types are needed to fully explain the observed differences in microbial community compositions observed in this study.

## Conclusions

Here, we investigated two Siberian thermokarst lakes with distinctly different (i) geographic settings (flat tundra vs. yedoma permafrost cliff) impacting the quantity and quality of sedimentary sources, as well as (ii) maximum lake depths (2.8 m vs. 6.9 m) impacting the prevailing ice regime and subsequently lake sediment temperatures in winter.

The floating-ice lake near the permafrost cliff has high contributions in mineral sediments and receives OC of Late Pleistocene age while the bedfast-ice lake is likely dominated by soil-OM of modern origin. The  $\delta^{13}\text{C}_{\text{org}}$  and  $\delta^{13}\text{C}_{\text{DOC}}$  values of the floating-ice lake are higher than in the bedfast-ice lake, which we interpret as an indication for the presence of more degraded SOC in the floating-ice lake sediment likely due to both, higher rates in (microbial) OC degradation, and the input of older, already degraded OC from an eroding yedoma shoreline.

The diversity in geochemical parameters and carbon properties across the two lakes is also well reflected in the microbial community composition. The differences were particularly pronounced in the taxonomic groups responsible for methane cycling, which could potentially influence methane fluxes from thermokarst lakes.

The observed differences across the lakes are likely an expression of two main factors. Firstly, the different lake depths with associated ice regimes (Fig. 9) that likely led to conditions of reduced OM decomposition (bedfast-ice lake) vs. increased OM decomposition (floating-ice lake). Secondly, the source material from the different eroding shorelines (contemporary, organic-rich, peaty soil vs. Late Pleistocene-aged yedoma soil) was reflected in the lake sediment composition and thereby also the supply of nutrients and OM (Fig. 9), which are key drivers for the growth of microbial communities. Even though this study cannot quantify to what degree these two drivers impact the carbon dynamics and microbial communities in thermokarst lake sediments, they are likely the keys to understand how thermokarst lakes process OC.

In the future, a rising number of bedfast-ice lakes is expected to shift their ice regime to floating-ice, if the current trajectory of Arctic warming continues (Arp et al. 2012, 2016), this is highly likely to also increase levels of erosion along thermokarst lake shorelines. Both of these developments would likely

increase the level to which sedimentary OM decomposition in lake taliks can take place, which in turn might impact the potential for increasing GHG emissions from Arctic thermokarst lakes (Manasypov et al. 2022).

**Acknowledgements** Special thanks are due for the local field support in Siberia to Roman Petrov and Dr. Alexander Kononov from the Institute for Biological Problems of the Cryolithozone, Siberian Branch Russian Academy of Sciences, Yakutsk, Russian Federation and Tatyana Strioekova and her team from the Fisheries and Nature Inspection in Chokurdakh. We want to express our sincere thanks to Richard van Logtestijn from the Systems Ecology department and Suzanne Verdegaal from the Stable Isotope Laboratory both at the Vrije Universiteit Amsterdam for the  $\delta^{13}\text{C}$  analyses on the solid samples. The XRF-scanning and core splitting were supported by Rineke Gieles, Piet van Gaever and Riek Hennekamp at the NIOZ Institute. The grainsize and TGA analyses were supported by Unze van Buren and Martine Hagen from the Sediment Laboratory of the Vrije Universiteit Amsterdam. The DOC analyses were kindly supported by Cedric Morana from the KU Leuven, Belgium. Special thanks for the cargo shipment support go to Natalia Sidorenko from STS Logistics Benelux. Thanks are also due to Maria Scheel for her support with the microbial interpretations and the NMDS. The authors also thank the two anonymous reviewers and the editor Brian Branfireun for their improvements of the manuscript.

**Author contributions** The fieldwork was carried out and supported by OHM, JFD, JvH, SK, LBM and AG. The XRF analyses were carried out and processed by OHM and G-JR. The  $^{14}\text{C}$  sample preparation, analyses and processing were carried out by LW and OHM. The DOC analyses were carried out by SB and OHM. The microbial analyses were carried out by MHZ and RR and interpreted by RR, MHZ and CUW. The manuscript and figures were written and compiled by OHM and RR with contributions from all co-authors.

**Funding** This work was carried out under the program of the Netherlands Earth Science System Centre (NESSC), which was funded by the Dutch Ministry of Education, Culture and Science (OCW) (Grant No. 024.002.001). The authors also thankfully acknowledge the SIAM Gravitation Grant 024.002.002 and the Netherlands Polar Programme (NWO project id 866.16.042).

**Data availability** The sedimentological, geochemical and physical data of this study are available on DataverseNL (<https://doi.org/10.34894/NPT2CF>). The microbial data are available on the Sequence Read Archive (SRA) of the National Center for Biotechnology Information (NCBI) under the Bio-project PRJNA889575 (<https://www.ncbi.nlm.nih.gov/bioproject/PRJNA889575>).

## Declarations

**Competing interest** The authors declare that they have no conflict of interest.

**Open Access** This article is licensed under a Creative Commons Attribution 4.0 International License, which permits use, sharing, adaptation, distribution and reproduction in any medium or format, as long as you give appropriate credit to the original author(s) and the source, provide a link to the Creative Commons licence, and indicate if changes were made. The images or other third party material in this article are included in the article's Creative Commons licence, unless indicated otherwise in a credit line to the material. If material is not included in the article's Creative Commons licence and your intended use is not permitted by statutory regulation or exceeds the permitted use, you will need to obtain permission directly from the copyright holder. To view a copy of this licence, visit <http://creativecommons.org/licenses/by/4.0/>.

## References

- Ackroyd TNW (1957) Laboratory testing in soil engineering. Soil Mechanics Ltd, London
- Ågren GI, Bosatta E, Balesdent J (1996) Isotope discrimination during decomposition of organic matter: a theoretical analysis. *Soil Sci Soc Am J* 60:1121–1126. <https://doi.org/10.2136/sssaj1996.03615995006000040023x>
- Aniceto K, Moreira-Turcq P, Cordeiro RC et al (2014) Hydrological changes in West Amazonia over the past 6 Ka inferred from geochemical proxies in the sediment record of a floodplain lake. *Procedia Earth Planet Sci* 10:287–291. <https://doi.org/10.1016/j.proeps.2014.08.065>
- Arp CD, Jones BM, Lu Z, Whitman MS (2012) Shifting balance of Thermokarst lake ice regimes across the Arctic Coastal plain of northern Alaska. *Geophys Res Lett* 39:1–5. <https://doi.org/10.1029/2012GL052518>
- Arp CD, Jones BM, Grosse G et al (2016) Threshold sensitivity of shallow Arctic lakes and sublake permafrost to changing winter climate. *Geophys Res Lett* 43:6358–6365. <https://doi.org/10.1002/2016GL068506>
- Arsenault J, Talbot J, Brown LE et al (2022) Biogeochemical distinctiveness of peatland ponds, Thermokarst waterbodies, and lakes. *Geophys Res Lett* 49:1–13. <https://doi.org/10.1029/2021gl097492>
- Ballantyne CK (2018) Periglacial geomorphology. Wiley, Hoboken
- Biskaborn BK, Herzschuh U, Bolshiyarov DY et al (2013) Thermokarst processes and depositional events in a Tundra lake, northeastern Siberia. *Permafrost Periglacial Process* 24:160–174. <https://doi.org/10.1002/ppp.1769>
- Bokulich NA, Kaehler BD, Rideout JR et al (2018) Optimizing taxonomic classification of marker-gene amplicon sequences with QIIME 2's q2-feature-classifier plugin. *Microbiome* 6:1–17. <https://doi.org/10.1186/s40168-018-0470-z>
- Bouchard F, Francus P, Pienitz R, Laurion I (2011) Sedimentology and geochemistry of thermokarst ponds in discontinuous permafrost, subarctic Quebec, Canada. *J Geophys Res Biogeosci* 116:1–14. <https://doi.org/10.1029/2011JG001675>
- Bouchard F, MacDonald LA, Turner KW et al (2017) Paleolimnology of Thermokarst lakes: a window into permafrost landscape evolution. *Arct Sci* 3:91–117. <https://doi.org/10.1139/as-2016-0022>
- Cai C, Leu AO, Xie GJ et al (2018) A methanotrophic archaeon couples anaerobic oxidation of methane to Fe(III) reduction. *ISME J* 12:1929–1939. <https://doi.org/10.1038/s41396-018-0109-x>
- Chadburn SE, Aalto T, Aurela M et al (2020) Modeled microbial dynamics explain the apparent temperature sensitivity of wetland methane emissions. *Global Biogeochem Cycles* 34:1–28. <https://doi.org/10.1029/2020GB006678>
- Colby GA, Ruuskanen MO, St.Pierre KA et al (2020) Warming climate is reducing the diversity of dominant microbes in the largest high Arctic lake. *Front Microbiol* 11:1–12. <https://doi.org/10.3389/fmicb.2020.561194>
- Coplen TB (1996) New guidelines for reporting stable hydrogen, carbon, and oxygen isotope-ratio data. *Geochim Cosmochim Acta* 60:3359–3360. [https://doi.org/10.1016/0016-7037\(96\)00263-3](https://doi.org/10.1016/0016-7037(96)00263-3)
- Cramer F (2021) Scientific colour maps (7.0.1). Zenodo. <https://doi.org/10.5281/zenodo.5501399>. Accessed 18 Oct 2022
- Davison W (1993) Iron and manganese in lakes. *Earth Sci Rev* 34:119–163. [https://doi.org/10.1016/0012-8252\(93\)90029-7](https://doi.org/10.1016/0012-8252(93)90029-7)
- de Jong AEE, in 't Zandt MH, Meisel OH et al (2018) Increases in temperature and nutrient availability positively affect methane-cycling microorganisms in Arctic thermokarst lake sediments. *Environ Microbiol*. 20:4314–4327. <https://doi.org/10.1111/1462-2920.14345>
- Dean JF, Meisel OH, Martyn Rosco M et al (2020) East siberian Arctic inland waters emit mostly contemporary carbon. *Nat Commun*. <https://doi.org/10.1038/s41467-020-15511-6>
- Duguay CR, Flato GM, Jeffries MO et al (2003) Ice-cover variability on shallow lakes at high latitudes: model simulations and observations. *Hydrol Process* 17:3465–3483. <https://doi.org/10.1002/hyp.1394>
- French HM (1996) The periglacial environment, 2nd edn. Addison Wesley Longman Limited, Harlow
- Grosse G, Jones BM, Arp CD (2013) Thermokarst lakes, drainage, and drained basins. In: Shroder JF (ed) *Treatise on geomorphology*. Elsevier, Amsterdam, pp 325–353
- Haroon MF, Hu S, Shi Y et al (2013) Anaerobic oxidation of methane coupled to nitrate reduction in a novel archaeal lineage. *Nature* 500:567–570. <https://doi.org/10.1038/nature12375>
- Hennekam R, Sweere T, Tjallingii R et al (2019) Trace metal analysis of sediment cores using a novel X-ray fluorescence core scanning method. *Quat Int* 514:55–67. <https://doi.org/10.1016/j.quaint.2018.10.018>
- Heslop JK, Walter Anthony KM, Winkel M et al (2020) A synthesis of methane dynamics in Thermokarst lake environments. *Earth Sci Rev*. <https://doi.org/10.1016/j.earscirev.2020.103365>
- Hinkel KM, Eisner WR, Bockheim JG et al (2003) Spatial extent, age, and carbon stocks in drained thaw lake basins on the Barrow Peninsula, Alaska. *Arctic Antarctic Alp Res* 35:291–300. <https://doi.org/10.1657/1523-0430>
- Hugelius G, Strauss J, Zubrzycki S et al (2014) Estimated stocks of circumpolar permafrost carbon with quantified uncertainty ranges and identified data gaps.

- Biogeosciences 11:6573–6593. <https://doi.org/10.5194/bg-11-6573-2014>
- in 't Zandt MH, Liebner S, Welte CU (2020) Roles of thermokarst lakes in a warming world. *Trends Microbiol* 28:769–779. <https://doi.org/10.1016/j.tim.2020.04.002>
- Iturrate-Garcia M, Heijmans M, Cornelissen JHC et al (2020) Plant trait response of tundra shrubs to permafrost thaw and nutrient addition. *Biogeosci Discuss*. <https://doi.org/10.5194/bg-2019-498>
- Jansen E, Christensen JH, Dokken T et al (2020) Past perspectives on the present era of abrupt Arctic climate change. *Nat Clim Change* 10:714–721. <https://doi.org/10.1038/s41558-020-0860-7>
- Jones BM, Arp CD (2015) Observing a catastrophic Thermokarst lake drainage in northern Alaska. *Permafrost Periglacial Process* 26:119–128. <https://doi.org/10.1002/ppp.1842>
- Jones BM, Grosse G, Arp CD et al (2011) Modern Thermokarst lake dynamics in the continuous permafrost zone, northern Seward Peninsula, Alaska. *J Geophys Res Biogeosci* 116:1–13. <https://doi.org/10.1029/2011JG001666>
- Jones SE, Zwart JA, Kelly PT, Solomon CT (2018) Hydrologic setting constrains lake heterotrophy and terrestrial carbon fate. *Limnol Oceanogr Lett* 3:256–264. <https://doi.org/10.1002/lol2.10054>
- Jongejans LL, Liebner S, Knoblauch C et al (2021) Greenhouse gas production and lipid biomarker distribution in yedoma and alas Thermokarst lake sediments in Eastern Siberia. *Glob Change Biol* 27:2822–2839. <https://doi.org/10.1111/gcb.15566>
- Kallistova AY, Kadnikov V, Savvichev AS et al (2021) Comparative study of methanogenic pathways in the sediments of Thermokarst and polygenetic Yamal lakes. *Microbiology* 90:261–267. <https://doi.org/10.1134/S0026261721020065>
- Katoh K, Standley DM (2013) MAFFT multiple sequence alignment software version 7: improvements in performance and usability. *Mol Biol Evol* 30:772–780. <https://doi.org/10.1093/molbev/mst010>
- Klindworth A, Pruesse E, Schweer T et al (2013) Evaluation of general 16S ribosomal RNA gene PCR primers for classical and next-generation sequencing-based diversity studies. *Nucleic Acids Res* 41:1–11. <https://doi.org/10.1093/nar/gks808>
- Kuhry P, Dorrepaal E, Hugelius G et al (2010) Short communication: potential remobilization of belowground permafrost carbon under future global warming. *Permafrost Periglacial Process* 21:208–214. <https://doi.org/10.1002/ppp.684>
- Lenz J, Jones BM, Wetterich S et al (2016) Impacts of shore expansion and catchment characteristics on lacustrine thermokarst records in permafrost lowlands, Alaska Arctic Coastal Plain. *Arktos* 2:1–15. <https://doi.org/10.1007/s41063-016-0025-0>
- Leu AO, Cai C, McIlroy SJ et al (2020) Anaerobic methane oxidation coupled to manganese reduction by members of the Methanoperedenaceae. *ISME J* 14:1030–1041. <https://doi.org/10.1038/s41396-020-0590-x>
- Ling F, Zhang T (2003) Numerical simulation of permafrost thermal regime and talik development under shallow thaw lakes on the Alaskan Arctic Coastal Plain. *J Geophys Res D Atmos*. <https://doi.org/10.1029/2002jd003014>
- Magnússon R, Limpens J, Kleijn D et al (2021) Shrub decline and expansion of wetland vegetation revealed by very high resolution land cover change detection in the Siberian lowland tundra. *Sci Total Environ* 782:146877. <https://doi.org/10.1016/j.scitotenv.2021.146877>
- Makri S, Wienhues G, Bigalke M et al (2021) Variations of sedimentary Fe and Mn fractions under changing lake mixing regimes, oxygenation and land surface processes during late-glacial and holocene times. *Sci Total Environ*. <https://doi.org/10.1016/j.scitotenv.2020.143418>
- Manasyypov RM, Lim AG, Krickov IV et al (2022) Carbon storage and burial in Thermokarst lakes of permafrost peatlands. *Biogeochemistry* 159:69–86. <https://doi.org/10.1007/s10533-022-00914-y>
- Matheus Carnevali PB, Herbold CW, Hand KP et al (2018) Distinct microbial assemblage structure and archaeal diversity in sediments of arctic Thermokarst lakes differing in methane sources. *Front Microbiol* 9:1–15. <https://doi.org/10.3389/fmicb.2018.01192>
- Matveev A, Laurion I, Deshpande BN et al (2016) High methane emissions from Thermokarst lakes in subarctic peatlands. *Limnol Oceanogr* 61:S150–S164. <https://doi.org/10.1002/lno.10311>
- McMurdie PJ, Holmes S (2013) Phyloseq: an R package for reproducible interactive analysis and graphics of microbiome census data. *PLoS ONE*. <https://doi.org/10.1371/journal.pone.0061217>
- Meisel OH, Dean JF, Vonk JE et al (2021) Porewater  $\delta^{13}\text{C}_{\text{DOC}}$  indicates variable extent of degradation in different talik layers of coastal Alaskan Thermokarst lakes. *Biogeosciences* 18:2241–2258. <https://doi.org/10.5194/bg-18-2241-2021>
- Morana C, Darchambeau F, Roland FAE et al (2015) Biogeochemistry of a large and deep tropical lake (Lake Kivu, East Africa: insights from a stable isotope study covering an annual cycle. *Biogeosciences* 12:4953–4963. <https://doi.org/10.5194/bg-12-4953-2015>
- Murton JB, Edwards ME, Lozhkin AV et al (2017) Preliminary paleoenvironmental analysis of permafrost deposits at Batagaika megaslump, Yana Uplands, northeast Siberia. *Quat Res (United States)* 87:314–330. <https://doi.org/10.1017/qua.2016.15>
- Nitzbon J, Westermann S, Langer M et al (2020) Fast response of cold ice-rich permafrost in northeast Siberia to a warming climate. *Nat Commun* 11:1–11. <https://doi.org/10.1038/s41467-020-15725-8>
- Oksanen J, Simpson GL, Blanchet FG (2022) Vegan: Community Ecology Package. R package version 2.5–7. Available at: <https://cran.r-project.org/web/packages/vegan/vegan.pdf>. Accessed 17 April 2022
- Price MN, Dehal PS, Arkin AP (2009) Fasttree: computing large minimum evolution trees with profiles instead of a distance matrix. *Mol Biol Evol* 26:1641–1650. <https://doi.org/10.1093/molbev/msp077>
- Qi H, Coplen TB, Geilmann H et al (2003) Two new organic reference materials for  $\delta^{13}\text{C}$  and  $\delta^{15}\text{N}$  measurements and a new value for the  $\delta^{13}\text{C}$  of NBS 22 oil. *Rapid Commun Mass Spectrom* 17:2483–2487. <https://doi.org/10.1002/rcm.1219>
- Reimer RW, Reimer PJ (2022) CALIBomb program. <http://calib.org>. Accessed 30 Sep 2022

- Reimer PJ, Brown TA, Reimer RW (2004) Discussion: reporting and calibration of post-bomb  $^{14}\text{C}$  data. *Radiocarbon* 46:1299–1304
- Reimer PJ, Austin WEN, Bard E et al (2020) The IntCal20 northern hemisphere radiocarbon age calibration curve (0–55 cal kBP). *Radiocarbon* 62:725–757. <https://doi.org/10.1017/RDC.2020.41>
- Schaller T, Wehrli B (1996) Geochemical-focusing of manganese in lake sediments - an indicator of deep-water oxygen conditions. *Aquat Geochem* 2:359–378. <https://doi.org/10.1007/bf00115977>
- Schirrmeister L, Grosse G, Wetterich S et al (2011) Fossil organic matter characteristics in permafrost deposits of the northeast Siberian Arctic. *J Geophys Res Biogeosci.* <https://doi.org/10.1029/2011JG001647>
- Schirrmeister L, Froese D, Tumskey V et al (2013) Yedoma: late Pleistocene ice-rich syngenetic permafrost of Beringia. *Encycl Quat Sci* 2nd Ed. <https://doi.org/10.1016/B978-0-444-53643-3.00106-0>
- Scholtysek G, Dellwig O, Roeser P et al (2020) Geochemical focusing and sequestration of manganese during eutrophication of lake Stechlin (NE Germany). *Biogeochemistry* 151:313–334. <https://doi.org/10.1007/s10533-020-00729-9>
- Schwaborn G, Andreev A, Rachold V et al (2000) Evolution of lake Nikolay, Arga island, western Lena river delta, during late Pleistocene and holocene time. *Polarforschung* 70:69–82
- Shaver GR, Chapin FS III (1991) Production: biomass relationships and element cycling in contrasting Arctic vegetation types. *Ecol Monogr* 61:1–31. <https://doi.org/10.2307/1942997>
- Siewert MB, Hanisch J, Weiss N et al (2015) Comparing carbon storage of siberian tundra and taiga permafrost ecosystems at very high spatial resolution. *J Geophys Res Biogeosci* 120:1973–1994. <https://doi.org/10.1002/2015JG002999>
- Simola H (1983) Limnological effects of peatland drainage and fertilization as reflected in the varved sediment of a deep lake. *Hydrobiologia* 106:43–57. <https://doi.org/10.1007/BF00016415>
- Strauss J, Schirrmeister L, Grosse G et al (2017) Deep Yedoma permafrost: a synthesis of depositional characteristics and carbon vulnerability. *Earth Sci Rev* 172:75–86. <https://doi.org/10.1016/j.earscirev.2017.07.007>
- Stuiver M, Reimer PJ (1993) Extended  $^{14}\text{C}$  data base and revised CALIB 3.0  $^{14}\text{C}$  age calibration program. *Radiocarbon* 35:215–230
- Thornton BF, Wik M, Crill PM (2015) Climate-forced changes in available energy and methane bubbling from subarctic lakes. *Geophys Res Lett* 42:1936–1942. <https://doi.org/10.1002/2015GL063189>
- Ulrich M, Jongejans LL, Grosse G et al (2021) Geochemistry and weathering indices of Yedoma and alas deposits beneath Thermokarst lakes in central Yakutia. *Front Earth Sci* 9:1–23. <https://doi.org/10.3389/feart.2021.704141>
- van Buuren U, Prins MA, Wang X et al (2020) Fluvial or aeolian? unravelling the origin of the silty clayey sediment cover of terraces in the Hanzhong Basin (Qinling Mountains, central China). *Geomorphology* 367:107294. <https://doi.org/10.1016/j.geomorph.2020.107294>
- van Huissteden J (2019) Methane and biogenic volatile organic compound emissions in Eastern Siberia. In: Ohta T, Hiyama T, Iijima Y, Kotani A, Maximov TC (eds) *Water-carbon dynamics in Eastern Siberia*. Springer, Singapore, pp 101–134. [https://doi.org/10.1007/978-981-13-6317-7\\_5](https://doi.org/10.1007/978-981-13-6317-7_5)
- van Huissteden J (2020) Thawing permafrost, permafrost carbon in a warming Arctic. Springer, Cham. <https://doi.org/10.1007/978-3-030-31379-1>
- van Huissteden J, Teshebaeva K, Cheung Y et al (2021) Geomorphology and InSAR-tracked surface displacements in an ice-rich Yedoma landscape. *Front Earth Sci* 9:1–21. <https://doi.org/10.3389/feart.2021.680565>
- Wacker L, Bonani G, Friedrich M et al (2010) Micadas: routine and high-precision radiocarbon dating. *Radiocarbon* 52:252–262. <https://doi.org/10.1017/S0033822200045288>
- Wacker L, Fahrni SM, Hajdas I et al (2013) A versatile gas interface for routine radiocarbon analysis with a gas ion source. *Nucl Instrum Methods Phys Res Sect B Beam Interaction Mater Atoms* 294:315–319. <https://doi.org/10.1016/j.nimb.2012.02.009>
- Walter KM, Zimov SA, Chanton JP et al (2006) Methane bubbling from siberian thaw lakes as a positive feedback to climate warming. *Nature* 443:71–75. <https://doi.org/10.1038/nature05040>
- Walter KM, Edwards ME, Grosse G et al (2007) Thermokarst lakes as a source of atmospheric  $\text{CH}_4$  during the last deglaciation. *Science* 318:633–636. <https://doi.org/10.1126/science.1142924>
- Walter Anthony KM, Zimov SA, Grosse G et al (2014) A shift of thermokarst lakes from carbon sources to sinks during the Holocene epoch. *Nature* 511:452–456. <https://doi.org/10.1038/nature13560>
- Walter Anthony K, von Schneider T, Nitze I et al (2018) 21st-Century modeled permafrost carbon emissions accelerated by abrupt thaw beneath lakes. *Nat Commun.* <https://doi.org/10.1038/s41467-018-05738-9>
- Walvoord MA, Voss CI, Ebel BA, Minsley BJ (2019) Development of perennial thaw zones in boreal hillslopes enhances potential mobilization of permafrost carbon. *Environ Res Lett.* <https://doi.org/10.1088/1748-9326/aaf0cc>
- Webb EE, Liljedahl AK, Cordeiro JA et al (2022) Permafrost thaw drives surface water decline across lake-rich regions of the Arctic. *Nat Clim Change.* <https://doi.org/10.1038/s41558-022-01455-w>
- Weiss N, Blok D, Elberling B et al (2015) Thermokarst dynamics and soil organic matter characteristics controlling initial carbon release from permafrost soils in the Siberian Yedoma region. *Sediment Geol.* <https://doi.org/10.1016/j.sedgeo.2015.12.004>
- Wik M, Thornton BF, Bastviken D et al (2014) Energy input is primary controller of methane bubbling in Subarctic lakes. *Geophys Res Lett* 41:555–560. <https://doi.org/10.1002/2013GL058510>
- Wik M, Varner RK, Anthony KW et al (2016) Climate-sensitive northern lakes and ponds are critical components of methane release. *Nat Geosci* 9:99–105. <https://doi.org/10.1038/ngeo2578>
- Windirsch T, Grosse G, Ulrich M et al (2020) Organic carbon characteristics in ice-rich permafrost in alas and Yedoma



- deposits, central Yakutia. *Sib Biogeosci* 17:3797–3814. <https://doi.org/10.5194/bg-17-3797-2020>
- Winkel M, Sepulveda-Jauregui A, Martinez-Cruz K et al (2019) First evidence for cold-adapted anaerobic oxidation of methane in deep sediments of Thermokarst lakes. *Environ Res Commun*. <https://doi.org/10.1088/2515-7620/ab1042>
- Yilmaz P, Parfrey LW, Yarza P et al (2014) The SILVA and “all-species living tree project (LTP)” taxonomic frameworks. *Nucleic Acids Res* 42:643–648. <https://doi.org/10.1093/nar/gkt1209>
- Zimov SA, Voropaev YV, Semiletov IP et al (1997) North siberian lakes: a methane source fueled by pleistocene carbon. *Science* 277:800–802. <https://doi.org/10.1126/science.277.5327.800>

**Publisher’s Note** Springer Nature remains neutral with regard to jurisdictional claims in published maps and institutional affiliations.